MESOSCOPIC AND GEOMORPHIC ANALYSIS ASSESSMENT OF CENOZOIC DEFORMATION IN THE NORTHERN WIND RIVER BASIN, CENTRAL WYOMING

A Thesis

Presented to

the Faculty of the Graduate School

at the University of Missouri-Columbia

In Partial Fulfillment

of the Requirements for the Degree

Master of Science

By

Ryan K. Owens

Dr. Francisco Gomez, Thesis Supervisor

DECEMBER 2024

The undersigned, appointed by the dean of the Graduate School, have examined the thesis entitled:

MESOSCOPIC AND GEOMORPHIC ANALYSIS ASSESSMENT OF CENOZOIC
DEFORMATION IN THE NORTHERN WIND RIVER BASIN, CENTRAL
WYOMING

presented by Ryan K. Owens,

a candidate for the degree of Master of Science,

and hereby certify that, in their opinion, it is worthy of acceptance.

Dr. Francisco Gomez

Dr. Nathan Hopkins

Dr. Tandis Bidgoli

ACKNOWLEDGEMENTS

I would like to begin by thanking my research advisor, Paco Gomez, for his exhaustive support and dedication directed toward this project. Thanks to my committee members Nate Hopkins and Tandis Bidgoli for their thorough feedback. Also, a huge thanks to Will Hunt for assisting with the field work in less-than-ideal conditions and in doing so, made this project possible. I would like to thank my brother, Ray Owens, as well as my aunt and uncle Ken and Sue Owens for their love and support during the completion of this thesis. Finally, thanks to the Department of Geological Sciences for their graduate student scholarship assistance and I also acknowledge the support received from the American Chemical Society's Petroleum Research Fund for my field studies.

Table of Contents

List of Figures

List of Tables

List of Equations

MESOSCOPIC AND GEOMORPHIC ANALYSIS ASSESSMENT OF CENOZOIC DEFORMATION IN THE NORTHERN WIND RIVER BASIN, CENTRAL WYOMING

Ryan K. Owens

Dr. Francisco Gomez Thesis supervisor

ABSTRACT

Within the northern Wind River Basin, just east of the Boysen Reservoir, the Stagner Creek Fault can be seen exposed within Quaternary gravel formations indicating that tectonic activity has occurred in the recent geologic history of the area. This is relative to the older tectonics of the region produced by Laramide age tectonism and responsible for the deeper tectonic structures such as the Shotgun Butte Thrust Fault. The local environment is sparsely populated. However, a threat to the dam of the Boysen reservoir as well as to the many oil and natural gas wells of the area exists which could have negative implications across the broader region. We used structure from motion (SFM) photography to develop DEMs and scarp profiles that show a 0.36m in the youngest surface that the fault cuts through and corresponds to a 6.3 magnitude quake. New and existing mesoscopic measurements show us that the region has experienced overall contraction. Schmidt hammer sampling helps confirm surface to age relationships in pre-Pinedale age surfaces but is not sensitive enough for post Pinedale age surfaces. The contraction explains the reverse sense of slip on the Stagner Creek Fault. From their relative positions, we also suggest that the Stagner Creek Fault at the surface and the Shotgun Butte Thrust at depth are most likely one in the same. This explains a reactivation of deeper, Laramide age structures

Chapter 1: Introduction

1.1 Background

The Wind River Basin lies between several Laramide age uplifts within central Wyoming. The Cenozoic basin stratigraphy consists of units formed from the deposition of material shed from these uplifts, as well as indications of late Cenozoic activity. Unlike the surrounding ranges, deformation contained in the basin is subtle and difficult to see even with current technology. As a result, post-Laramide deformation in the Wind River Basin is under studied and poorly understood.

The study focusses on the area around Birdseye Creek at the northern margin of the Wind River Basin (Figure 1-1). The area contains the remnants of an alluvial fan, the Birdseye Creek fan, along the southern front of the Owl Creek Mountains and east of Wind River Canyon. Although sometimes called the Bridger Range, this section of the mountain north of Birdseye Creek will be referred to as the central Owl Creek Mountains in this thesis. The mountain, just north of the field site in Figure 1-1, forms a large anticlinorium.

The Boysen reservoir can be seen to the west from the field site with the naked eye as it is less than 5km to the water's edge (Figure 1-1). The trace of the fault in the northwest direction points in the vicinity of the dam that holds back the water within the reservoir. This could be of concern were significant seismic activity to occur here as this water supply serves a more significant population downstream. The population of the local area is minimal as only a few ranchers inhabit the area. However, the oil and gas industry has taken an interest here as a number of wells have been put in place for extraction purposes. Damage to these wells would have financial implications for both owners and local industry. Above all else, the danger to the environment is the greatest concern. Since the reservoir is in such close proximity, contamination of the water table is the worst-case scenario as it would most likely spread to the reservoir.

Within the Birdseye Creek alluvial fan complex lie Quaternary deformation features. These structures are a mixture of east-west striking normal and reverse faults. Subtle warping of the Cenozoic bedrock at the surface is also apparent. Many of the deformation structures around Birdseye Creek have been mapped previously (Thaden 1978, 1980).

The primary goal of this investigation is the analysis of Quaternary deformation and how it relates to deeper bedrock structures. The Stagner Creek Fault, which can be seen in map view in Figure 1-2 and the photograph in Figure 1-3, will aid with this. The fault cuts across Quaternary gravels of the alluvial fan but dissipates toward the northwest when it encounters the creek bed where active deposition is apparent. The trace toward the southeast is eventually lost as it too encounters younger gravel surfaces and active alluvium.

1.2 Objectives

There are three hypothesis I wish to test during this investigation:

1. The Stagner Creek Fault is a reverse fault (i.e., horizontal contraction).
2. The trace of the Stagner Creek Fault cuts across younger surfaces than previously documented.
3. The trace of the Stagner Creek Fault continues in both the northwest and southeast directions beyond the active alluvium that buries it in specific locations.

To test these hypotheses, this study aims to look at several aspects of the field area:

1. New bedding attitudes will be combined with existing map data in order to develop one or more cross sections containing the fault. The cross section(s) will be examined for evidence of contraction.
2. Higher resolution DEMs than what is publicly available will be developed through the use of UAS and RTK technology in the areas where the fault trace diminishes. The DEMs will show us if the scarp can be traced further than previously mapped. Scarp profiles will also be developed from the new DEMs to examine how the fault interacts with younger surfaces that are suspected of having no deformation.
3. Schmidt hammer samples will be analyzed to supplement the scarp profiles with relative ages. The relative ages found here will be compared to soil age estimates from previous work.
4. After all data has been collected and analyzed, a comparison of Quaternary and bedrock deformation will be made to investigate possible links between the two.

Chapter 1 Figures

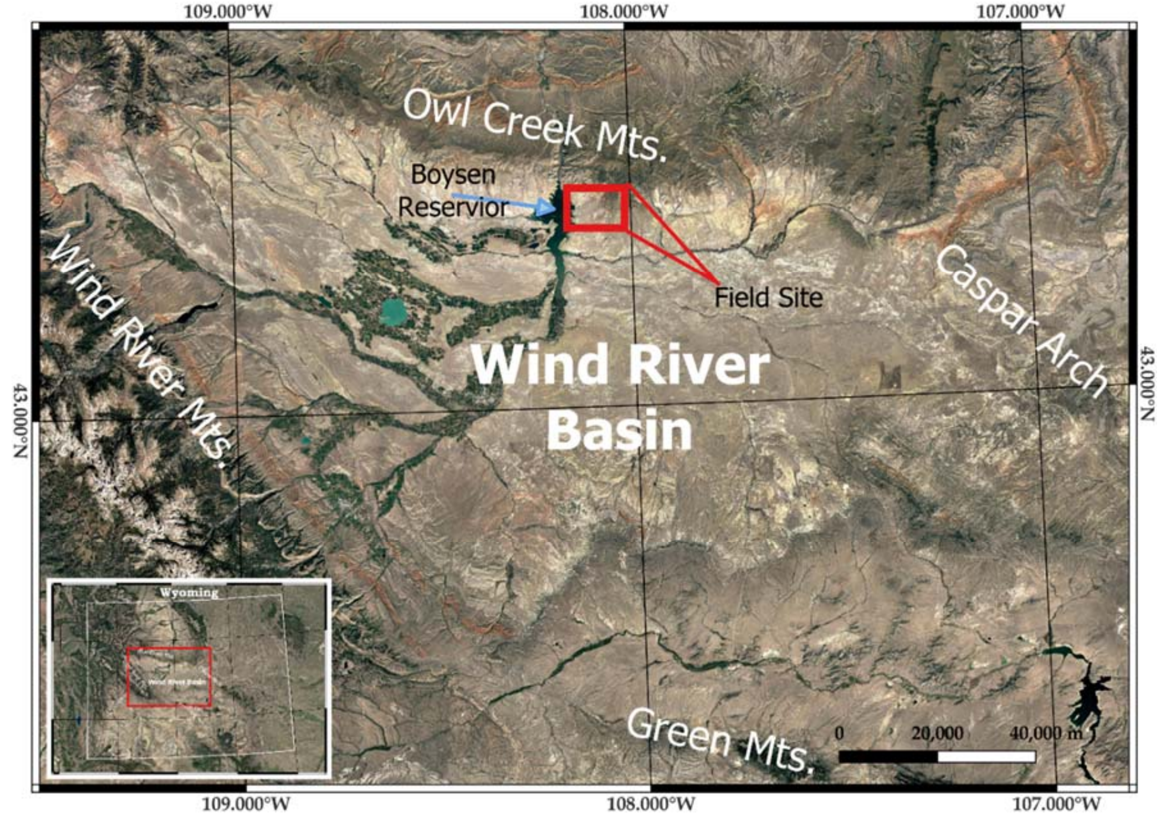

Figure 1-1. Wind River Basin with the major features surrounding that surround it. The field site is outlined in red on the main map. The inset map outlines Wyoming with the red box in it outlining the main map.

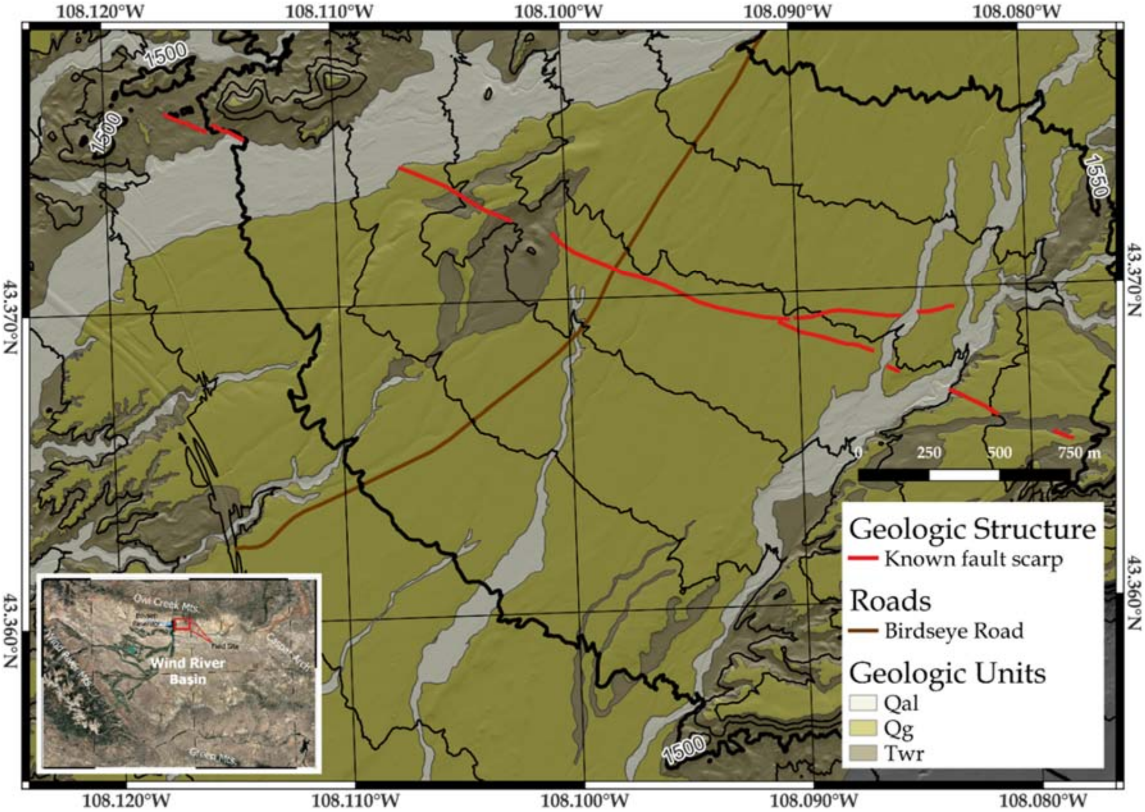

Figure 1-2. The area of focus at the field site displaying the Stagner Creek Fault across Birdseye Creek, a key geologic structure. Inset map from Figure 1-1

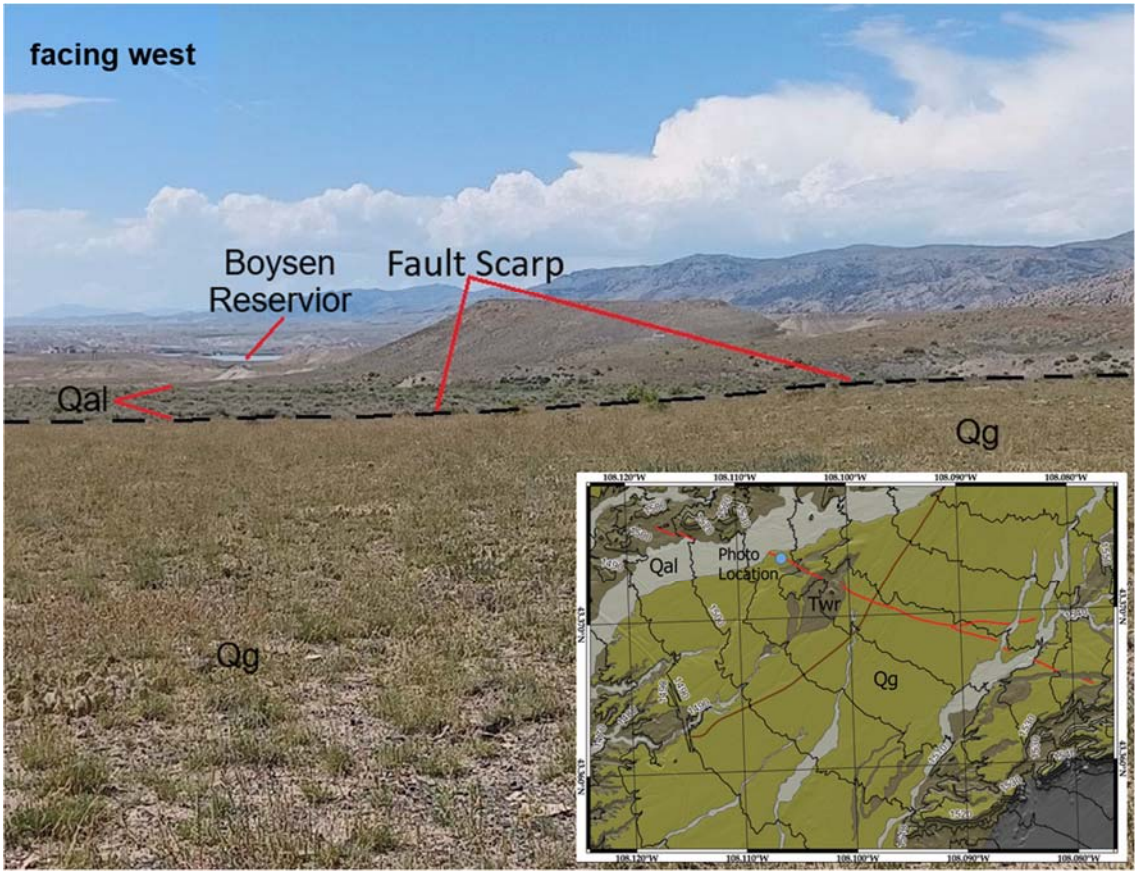

Figure 1-3. A photograph of the fault scarp at Birdseye Creek. The blue dot on the inset denotes the photograph location.

Chapter 2 Geologic Background

Beginning in the late Cretaceous (~80 Ma), a significant deformation event began causing horizontal contraction and uplift of the area. Often called the Laramide Orogeny (Allmendinger, 1992), the Owl Creek Mountains were a result of this. With Mesozoic and Paleozoic units in place, down warping of the present-day location of the Wind River Basin initiated at the same time. This deformation ended in the early Eocene (~55 Ma) producing the high range of the Owl Creeks uplifted on a reverse fault and the deep Wind River Basin to the south that coincides with the range (Keefer, 1970). This uplift is what initiated the erosion of the range causing material to shed south into the Wind River Basin and developed the formations of the early Eocene (Soister, 1968).

2.1 Plate Tectonic Setting of Western North American Continent

The initiation and driving force behind the Laramide Orogeny is a process called flat-slab subduction. In more typical subduction processes, a uniform dipping angle of the subduction plate is categorized around 30° (Horton et al, 2022). This does not explain the formation of the Laramide uplifts which exist far within the interior of the North American Continent. A shallow-subduction system, on the other hand, can better explain interior plate deformation where this explanation focusses on contraction rather than vertical uplift (Allmendinger, 1992). Other evidence for the flat-slab subduction at this time is the lack of subduction-related volcanism along the margin of western North America.

The evolution of the plate boundary is shown in Figure 2-1A, when the Farallon plate begins the subduction process around 90 Ma at the expected angle of around 30°. In Figure 2-1B, the plate levels off while continuing to travel underneath the North

American plate. Figure 2-1C shows the plate resuming it's 30° downward trend but not before deforming the North American plate above during the Paleocene in Figure 2-3B. Figure 2-2 Is a progression of maps of western North America that supplements the cross sections of the plate subduction process and the block diagrams of the Wind River Basin progression in Figures 2-1 And 2-3 respectively. This explains the deep basins found out in front of the thrusted blocks of the ranges. Regional shortening in the fold thrust belt causes loading and flexure at the margin between the range and basin (Horton et al, 2022). The Wind River Basin at the base of the Owl Creek Mountains is no exception as can be seen in Figure 2-8 where Tertiary sediments are near three km thick.

The Laramide Orogenic event ends during the Eocene where erosion of the ranges picks up significant speed as they dump their sediment into the corresponding basins. Erosional processes continue through the Eocene with the ranges being planated and stream incision removing the more erodible sediments in the basin while at the same time excavating the more competent crystalline layers of the range (Glass, 1986). Western North America experiences a period of epeirogenic uplift and a repeat of basin filling occurs during the Oligocene and Miocene (Glass, 1986). The process cycles back around to stream incision and removal of sediments during the Quaternary which is ongoing today.

2.2 Bedrock Stratigraphy

Within the field site of this investigation, there are three bedrock formations that outcrop. These are the Madison Limestone, Wind River, and Wagon Bed formations. The Madison is seen toward the north where the basin gives way to the foot of the mountain. The Wagon Bed has spotty outcrops toward the east. The Wind River outcrops most other places in the basin that the Wagon Bed does not when it is not buried by Quaternary deposition (Thaden 1978, 1980). The Wind River formation rests unconformably on top of the Madison Limestone at the surface in Figure 2-7. Moving south from this location at the base of the mountain, the basin thickens and other units begin to appear. This is apparent in a well log where Mesozoic units of the Mesaverde, Cody, and Frontier among others were recorded being drilled through (CIG Exploration, 1978). To understand the bedrock stratigraphy at depth, see Figure 2-5 and 2-6.

Cenozoic Bedrock

There are three formations that are syntectonic or post Laramide in age that exist at the field site. Two of the three, the Wind River and Wagon Bed formations, outcrop here. The Fort Union syntectonic formation exists but can only be found within well logs in the footwall of the range-bounding fault buried below the two previously mentioned units. The Wind River and Wagon Bed act as the capping formations of the bedrock in the basin at the location of the field site.

Wind River Formation

Early Eocene in age, (Soister, 1968) the Wind River formation is the capping bedrock formation within the Wind River Basin at the field site. This formation contains a host of interbedded claystone, siltstone, sandstone, and conglomerate layers with an arkosic lithology (Soister, 1968). A second, yet similar description is that this formation consists of "lenticular deposits of poorly sorted yellowish feldspar-rich sandstone commonly containing calcareous limonitic cement, poorly sorted pebble conglomerate, and red-banded mudstone, as well as local layers of carbonaceous shale and a few coal beds" (Wyoming Geological Association, 1964). At the field site, this formation lies unconformably on top of Paleozoic units at the base of the range. Thickness of the formation varies depending on the location within the basin. Figure 2-8 shows a cross section by Blackstone (1990) that estimates the thickness of the Wind River formation south of the Owl Creek Mountains to be around 1000 m thick. The variation of interbedding from clays and silts to pebble conglomerates seen at the field site and described above fits that of a lakeshore environment. Figure 2-4 shows an example of a lakeshore environment that receives sediment input from a nearby alluvial fan system. Dominant features are the wide assortment of clast size and the channel deposits containing large amounts of sand. Although transgressive and regressive cycles were not explicitly sought out in the field, the explanation of their appearance is one of constant change of material input. Furthermore, this suggests an environment that is highly susceptible to change.

Wagon Bed Formation

This formation overlays the Wind River formation and is described as being a host of volcaniclastic claystone and sandstone deposits in the description for the unit in GQ-1527 (Thaden, 1980). The Wyoming Geological Association (1964) describes the sediment between the Wind River and White River formations as volcanic-rich rock. Although it is only referred to as Middle to Upper Eocene in age, this is the Wagon Bed. This formation does not outcrop at the field site where new mesoscopic measurements were taken, but does show up in the eastern sections of the map area in QG-1527 (Thaden, 1980).

2.3 Major Tectonic Structures

East Owl Creek Mountains

The range of the Owl Creeks north of Birdseye Creek is the dominant geologic feature of the area and can be observed in Figure 2-7 in cross section. This cross section is very useful as it not only crosses the field site of this investigation, but also displays the location in the mountain range where the tilt direction of the bedding planes changes from north to south. By viewing the cross section, the Owl Creek Mountains are seen in the shape of an anticlinorium structure with its hinge pointing in the relative east/west directions. Also, Mesozoic and Paleozoic units of the southern limb are extensively broken up due to a vast system of faults. Many of these faults align sub-parallel with the hinge of the fold and this system of faulted units continues south into the post Laramide formations of the Wind River Basin south of the mountain range.

South Owl Creek Thrust Fault

This fault is given various names in the literature it is included in and is the key structure in uplifting the Owl Creek Mountain Range. Keefer, 1970 identifies this as the South Owl Creek Mountains Fault where Blackstone, 1990 labels it as the Owl Creek Thrust Fault. This investigation will use the phrase South Owl Creek Thrust Fault to avoid confusion with the North Owl Creek Thrust Fault. The fault's orientation has a couple of interpretations. It is widely agreed upon that the fault dips in the northern direction. However, the angle at which it dips is what is debated. One interpretation is that the fault dips 30 to 40 degrees (Blackstone, 1990, pg. 157). A second interpretation that heavily contrasts the first is that the fault dips at an angle much higher, around 70 to 80 degrees (Wise, 1963; Keefer, 1970). The reason for this debate is that the fault does not break through to the surface, it is overlain by the Wind River formation (Keefer, 1970; Blackstone, 1990). Blackstone estimates the total amount of slip on the fault at 10,970 meters.

Shotgun Butte Thrust Fault

The eastern extension of the Shotgun Butte Thrust Fault contributes to the uplift of the Owl Creek Mountains (Bader, 2018). Figure 2-9 shows this fault is just north of the South Owl Creek Thrust Fault. Blackstone has also produced a cross section that is represented in Figure 2-8 that agrees with the positioning of the two faults in the corresponding map in Figure 2-9. In the map, both faults are dashed including within the field site of this investigation meaning their location is inferred. This makes it difficult to position these two structures on a localized level. What we can say is that the Shotgun Butte Thrust Fault continues west where it becomes visible in the basin. Towards the east, this fault is shown to die out. Both Blackstone and Bader agree with this east/west positioning.

Boysen Normal Fault

The Boysen Fault runs relatively parallel and just north of the hinge of the main anticlinorium of the range seen in Figure 2-7. It is a normal fault with the northern block representing the foot wall and the southern block representing the hanging wall. There are few other deformation structures in the form of faults north of the Boysen Fault. In comparison, there are numerous other minor fractures southward that continue down into the basin while all remaining relatively parallel to the hinge of the anticlinorium. The area south of Boysen Fault is referred to as the toe of the thrust (Blackstone, 1990). Keefer, 1970 describes this as tensional fracturing of rigid rocks and Wise, 1963 describes it as the overhanging lip of the thrust. Blackstone supports a sequence of thrusting followed by developing normal faults and the collapse of the toe of the thrust. Wise supports a mechanism that tries to explain how reverse and normal faulting occurred simultaneously. The mechanism involves the thrust block moving over sediments of varying strength. Keefer, 1970 attempts to explain that the tensional fracturing developed during the uplift with these fractures propagating for some time after orogenic uplift had ceased. All three papers use the Boysen Fault as evidence. Stratigraphic displacement on the fault is estimated at around 609 m (Blackstone, 1990,).

2.4 Quaternary Deposits

Gravels

Quaternary gravel deposits in the map area are the remnants of older alluvial fan systems shed from the Owl Creek Mountains during late Cenozoic exhumation. The grain size ranges from boulder to silt and has an average clast size increasing as distance from the mountain decreases (Thaden, 1978). Thaden's description continues with rock types ranging from the dominant Precambrian hornblende-plagioclase granites with good amounts of various schists, quartzite, and even small amounts of limestones of Carboniferous age and older. In many cases, these gravel surfaces are slightly elevated above the surrounding Wind River formation and Quaternary Alluvium deposits. See Thaden 1978, 1980 for examples in the cross sections provided on the maps. A seismotectonic evaluation of the northwestern Wind River basin agrees with the variation of rock types with an addition of dolomitic rock that is probably of the same origin as the limestone found here (Geomatrix Consultants, 1988). This evaluation breaks down the

Late Quaternary alluvial units at Birdseye Creek into 6 separately aged surfaces, the five oldest classified as gravels in Figure 2-10.

Surface Q1

This surface shows “distinct evidence of displacement” across the fault at the field site (Geomatrix Consultants, 1988). A significant desert pavement exists with 80% of the surface covered in interlocking pebble and coble clasts. The non-calcareous rock types possess a well-developed desert varnish where calcareous clasts are quite pitted. Exact displacement across the fault is difficult to determine but is suggested to be over 2 m (Geomatrix Consultants, 1988, pg. 41).

Surface Q2

50-60% of surface Q2 contains similar clast sizes as Q1 but has a greater spread and are not interlocking. A desert varnish is present in similar fashion to Q1 and displacement across the fault is estimated at 2.2 m (Geomatrix Consultants, 1988).

A numerical age of 30-60 ka has been suggested for this surface by relating it to soils found in Pinedale age soils which are no more than 30 ka. Based on pedogenic carbonate accumulation, a numerical age of 30-60 ka has been suggested. This buildup is greater in surface Q2 soils than in post-Pinedale soils at Bull Lake and because of this, it is most likely that surface Q2 is older than the post-Pinedale soils (Geomatrix Consultants, 1988).

Surface Q3

This surface contains a moderate desert pavement but is discontinuous. Areas where the pavement is most prevalent have a clast coverage of 40-50%. A desert varnish continues to cover the non-calcareous clasts and displacement on the fault is approximately 1 m (Geomatrix Consultants, 1988). A numerical age of 15-40 ka has been suggested for this surface by relating it to Pinedale age soils. The report again uses carbonate morphology, which it explains is comparable to but may be slightly older than that of the post-Pindale carbonate buildup at Bull Lake. Because of this, surface Q3 is comparable in age to the post-Pinedale age soils (Geomatrix Consultants, 1988).

Surface Q4

This surface is described as a localized area due to stream incision. Its appearance is much the same as surface Q3 but vertical displacement across the fault only measures 0.5 m. The scarp angle differs from the three older surfaces as well (Geomatrix Consultants, 1988). A numerical age of 8-20 ka has been suggested for this surface. However, the report bases this number only off of the well-developed bar and swale morphology and its relation to surfaces Q2 and Q3 which have some of the same morphology but not as clear as surface Q4 (Geomatrix Consultants, 1988).

Surface Q5

The desert pavement is poorly developed here. Non-calcareous clasts contain a desert varnish only atop the raised areas of the surface where the pavement has partially developed. The displacement across the fault is non-existent at this surface (Geomatrix Consultants, 1988). This would indicate that surface Q5 developed after fault propagation had stopped. However, DeLisle et al, 2016 developed a DEM centered on the Stagner Creek Fault at Birdseye Creek where the fault can be seen cutting through the Q5 surface. This indicates that the fault is actually younger that surface Q5. A relative age of 1-7 ka has been suggested for this surface. Like surface Q4, surface Q5's age is based on the bar and swale morphology in the report. It is placed as younger than surface Q4 with its lack of degradation in the bar and swale deposition (Geomatrix Consultants, 1988).

Alluvium

The alluvium of the Quaternary is composed of sand of fine to very fine quarts grains with a quarter of the sediment being silt and clay. Another three percent is composed of accessory minerals which are mostly garnet, ferromagnesian grains, and mica flakes (Thaden, 1980). From the quadrangle maps by Thaden in the area of the field site, you can see that the alluvium is mostly confined to the small streams and waterways. In the Geomatrix Consultants' Birdseye Creek study area, surface Q6 is actually the Quaternary alluvium in their descriptions. Bar-and-swale topography persists and clasts commonly have desert varnish consistent with higher surfaces, most likely due to the varnish not being destroyed during transport (Geomatrix Consultants, 1988). The report goes on to explain in the description of surface Q6 and the map of the gravel surfaces that it is not deformed by the Stagner Creek Fault suggesting that the last faulting event occurred before the alluvium was deposited.

Identified by Geomatrix Consultants as surface Q6, this surface is the area of active deposition. To distinguish it from surfaces Q1-Q5 and to prevent any confusion, Geomatrix's Q6 is not a gravel surface. This is classified as alluvium and is composed of sand of fine to very fine quarts grains with a quarter of the sediment being silt and clay. Another three percent is composed of accessory minerals which are mostly garnet, ferromagnesian grains, and mica flakes (Thaden, 1980). From the quadrangle maps by Thaden, you can see that the alluvium is mostly confined to the small streams and other waterways. Bar-and-swale topography persists and clasts commonly have desert varnish consistent with higher surfaces, most likely due to the varnish not being destroyed during transport (Geomatrix Consultants, 1988). In Figure 2-10, you can see that the fault does not deform the Quaternary alluvium suggesting that the last faulting event occurred before the alluvium was deposited.

2.5 Quaternary Tectonism

Information about the geologically recent deformation found in the Birdseye Creek area is minimal. There has been an evaluation of Stagner Creek Fault at Birdseye Creek as well as a study at Jewell Creek approximately four km west of the Boysen Reservoir (Geomatrix Consultants, 1988). However, these two study areas only investigate this fault zone and the surfaces it cuts through. The evaluation at Birdseye Creek describes the amount of displacement caused by the fault but does not go into detail about the fault's orientation or direction of slip. The orientation is relatively north dipping and the slip on the fault seems to be of reverse nature where a possible reactivation of the fault has occurred (Gomez et al, 2016). A shallow seismic reflection profile was created from a seismic line done measuring 420 meters across the Q3 surface and using a Betsy gun as the seismic source (Abousaif, 2012). The image produced can be seen in Figure 2-11 and easily displays a break in strata indicated by the black arrows with a reverse sense of motion within the Wind River formation underlying the gravel surfaces.

The major gap in the literature is the absence of information about folding or warping of the basin fill units near Birdseye Creek. Markers identifying anticline/syncline folds exist in Thaden's quadrangle maps across Quaternary surfaces, but explanations for these are not discussed anywhere. The topic is lightly discussed in the study by Gomez et al, 2016 where Gomez argues that the cause of the fault is a result of folding rather than faulting and displacement.

Chapter 2 Figures

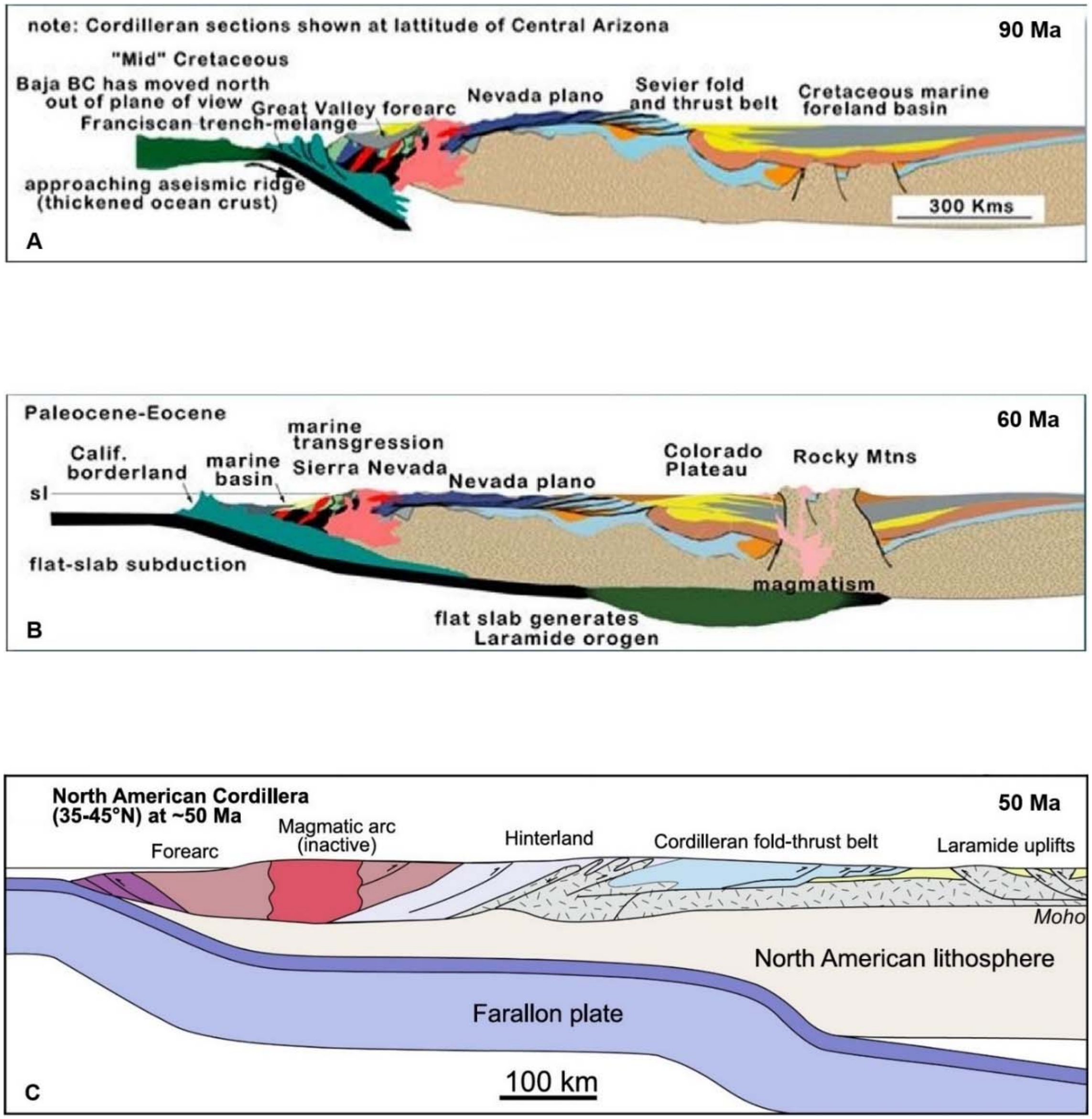

Figure 2-1. A. Cross section of the North American Cordillera showing onset of subduction of the Farallon Plate (Blakely, 2013). **B.** Cross section showing progressed subduction and indication of flat-slab processes (Blakely, 2013). **C.** Cross section showing flat-slab subduction and resulting deformation in the foreland (Horton et al., 2022).

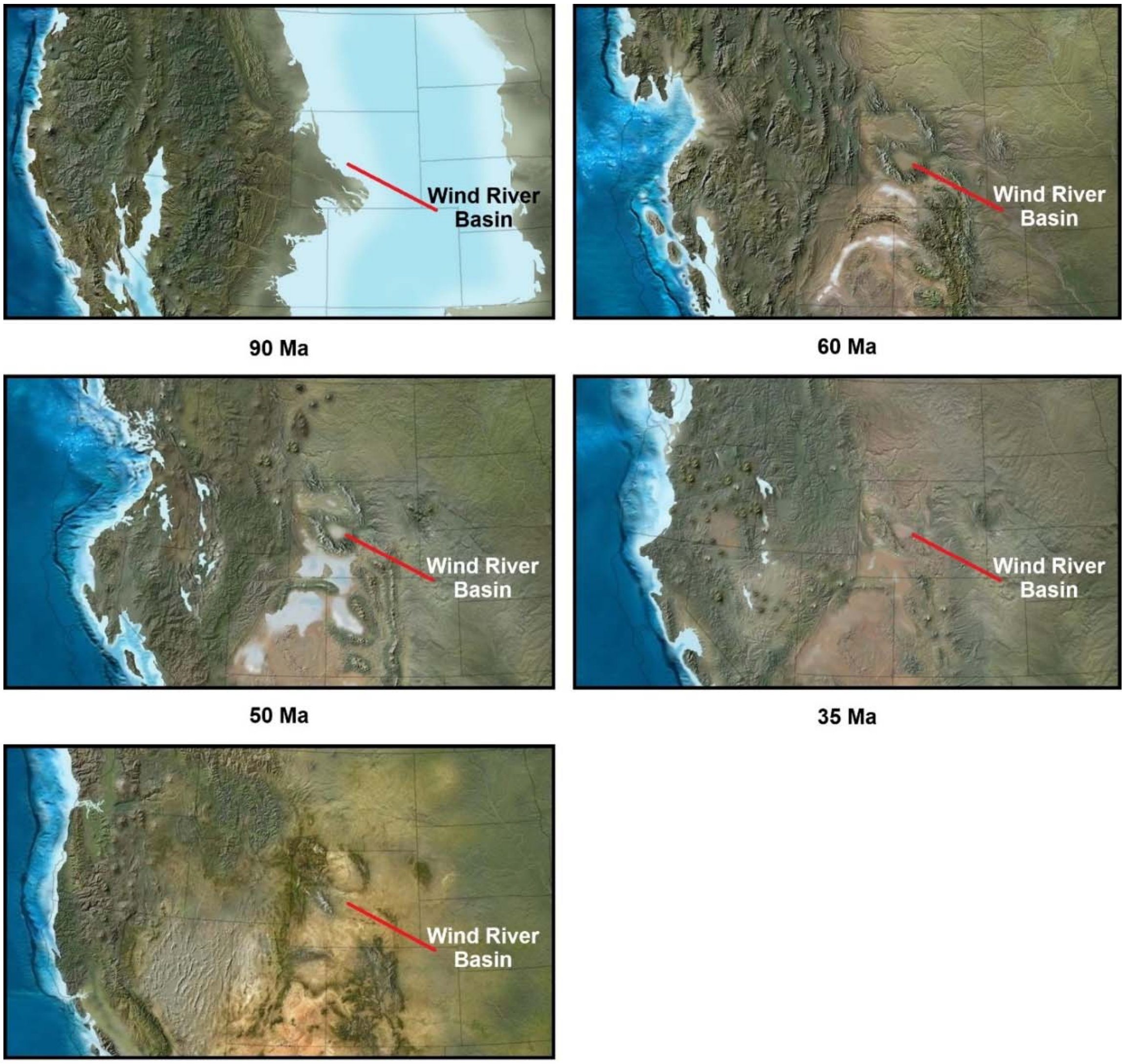

90 Ma

60 Ma

50 Ma

35 Ma

05 Ma

Figure 2-2. Geologic evolution of the Western U.S. in relation to the Wind River Basin. Maps taken and adapted from Blakely (2013).

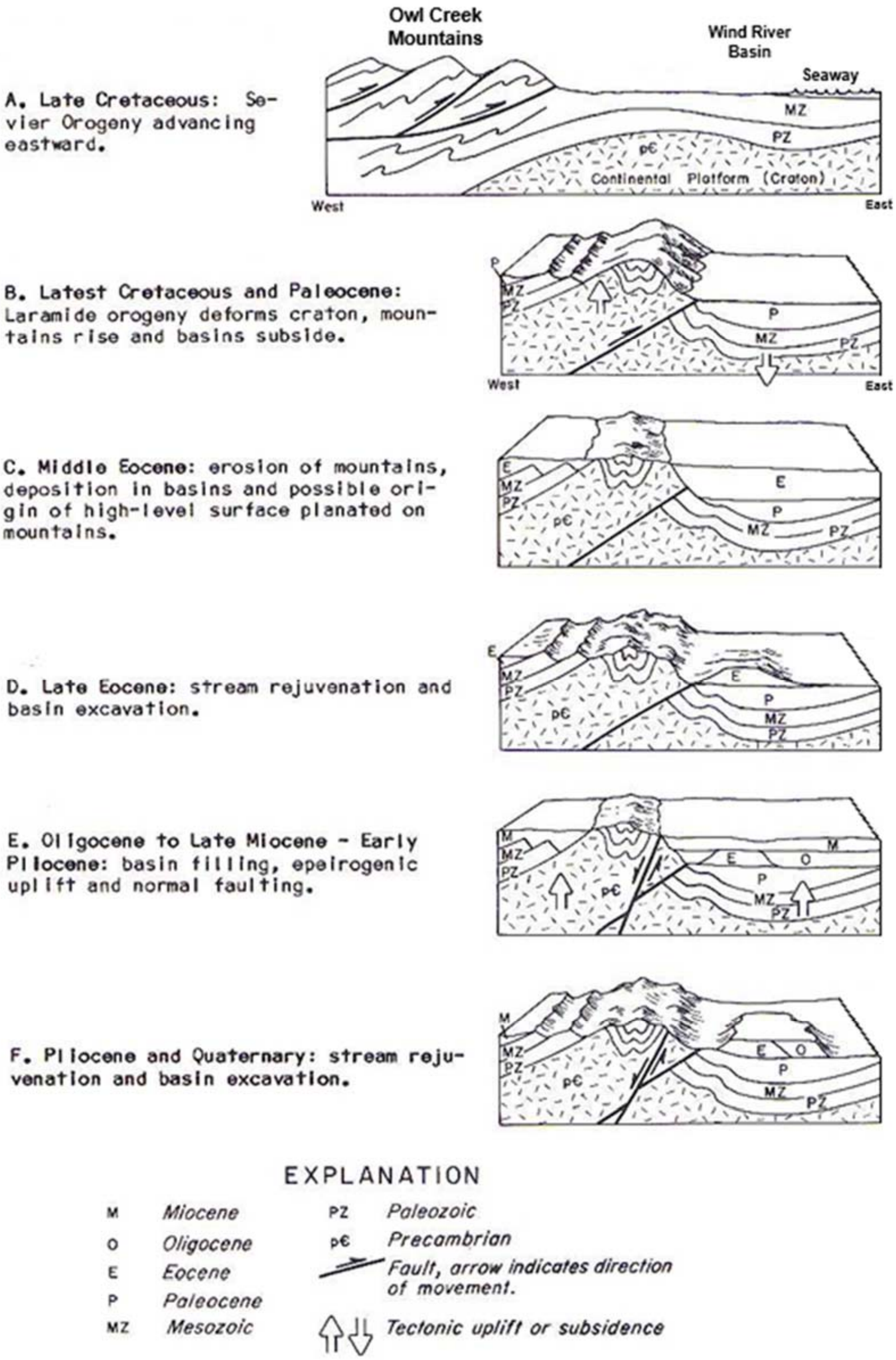

Figure 2-3. Geologic evolution of the Wind River Basin. Block diagrams taken and adapted from Glass (1986).

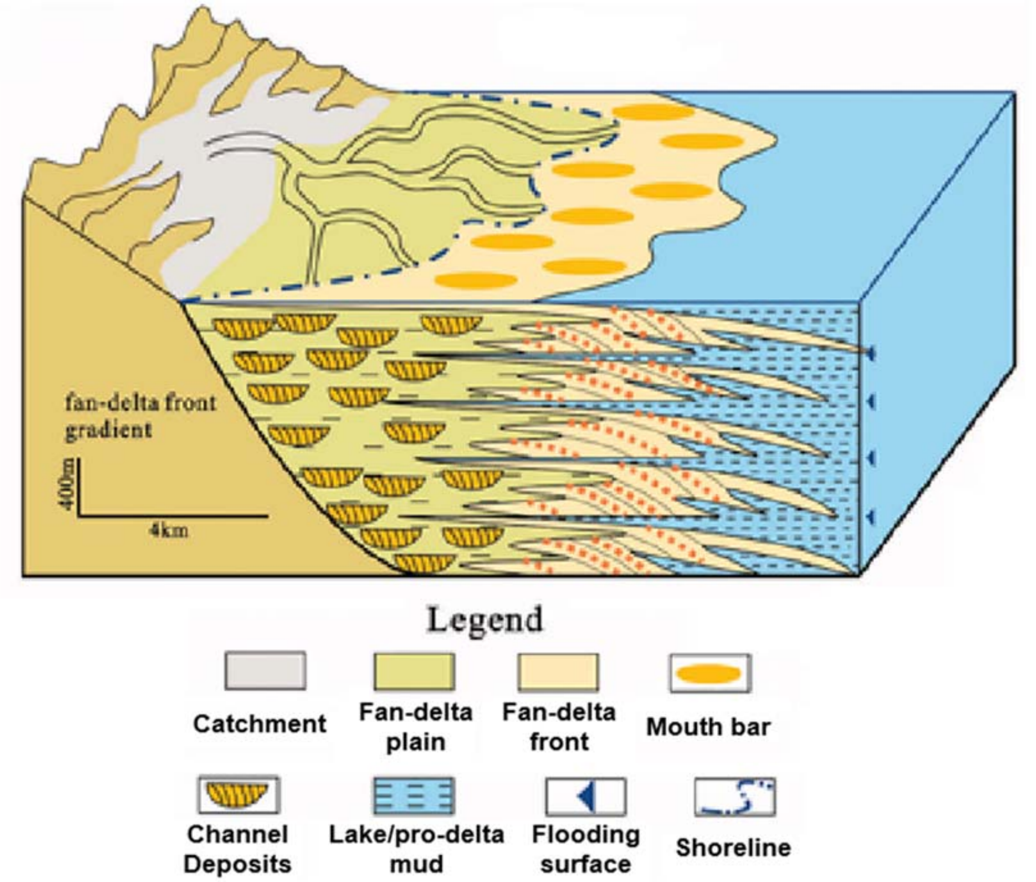

Figure 2-4. A. Block Diagram and facies model of an alluvial fan/lakeshore environment. Notice the presents of intermittent channel deposits from the migrating stream system. Taken and adapted from Jia et al. (2021).

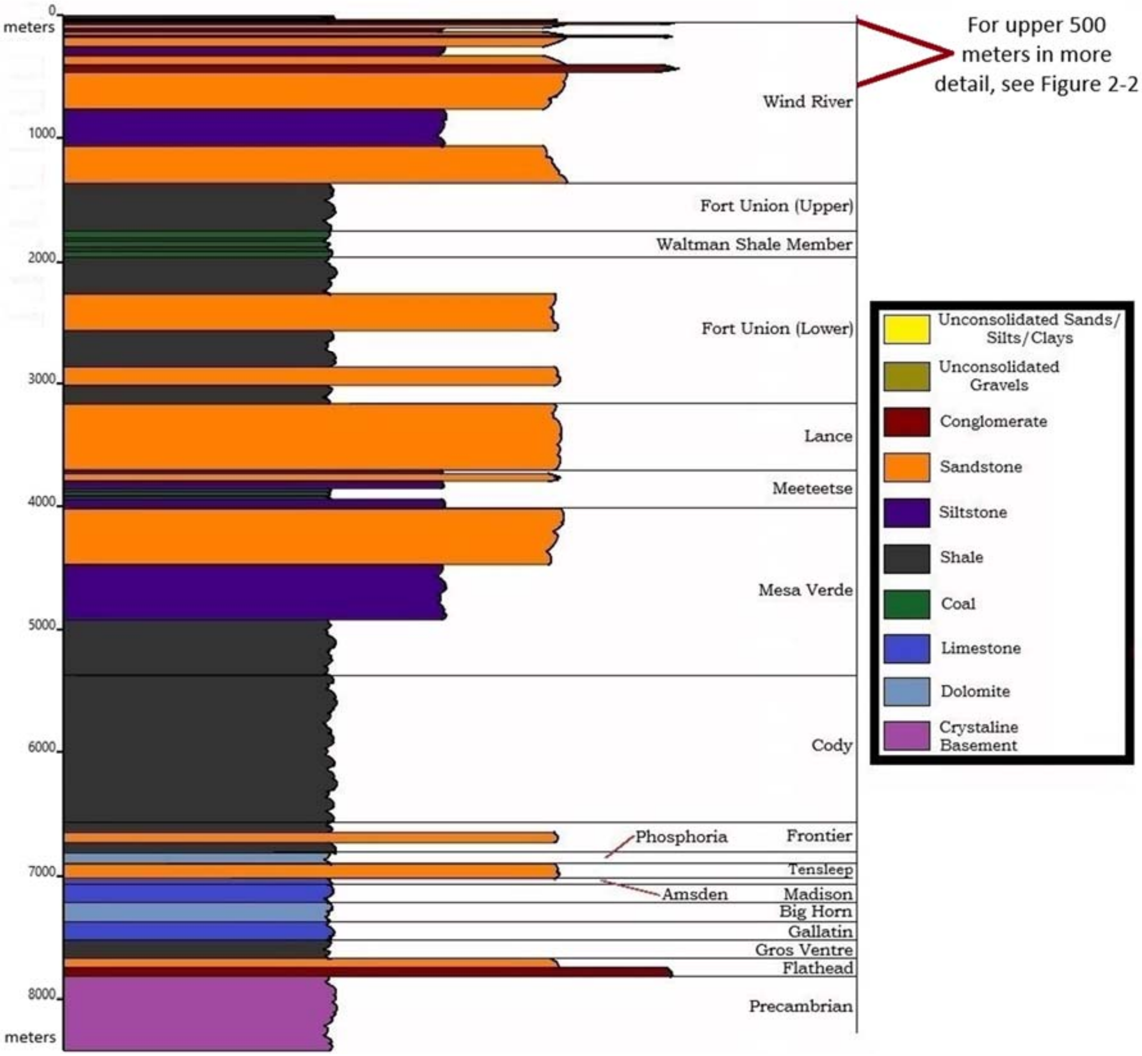

Figure 2-5. The stratigraphy of the Wind River Basin at Birdseye Creek from the surface to the crystalline basement. Thicknesses based on several well logs at various locations in the surrounding area of Birdseye Creek and may vary depending on location.

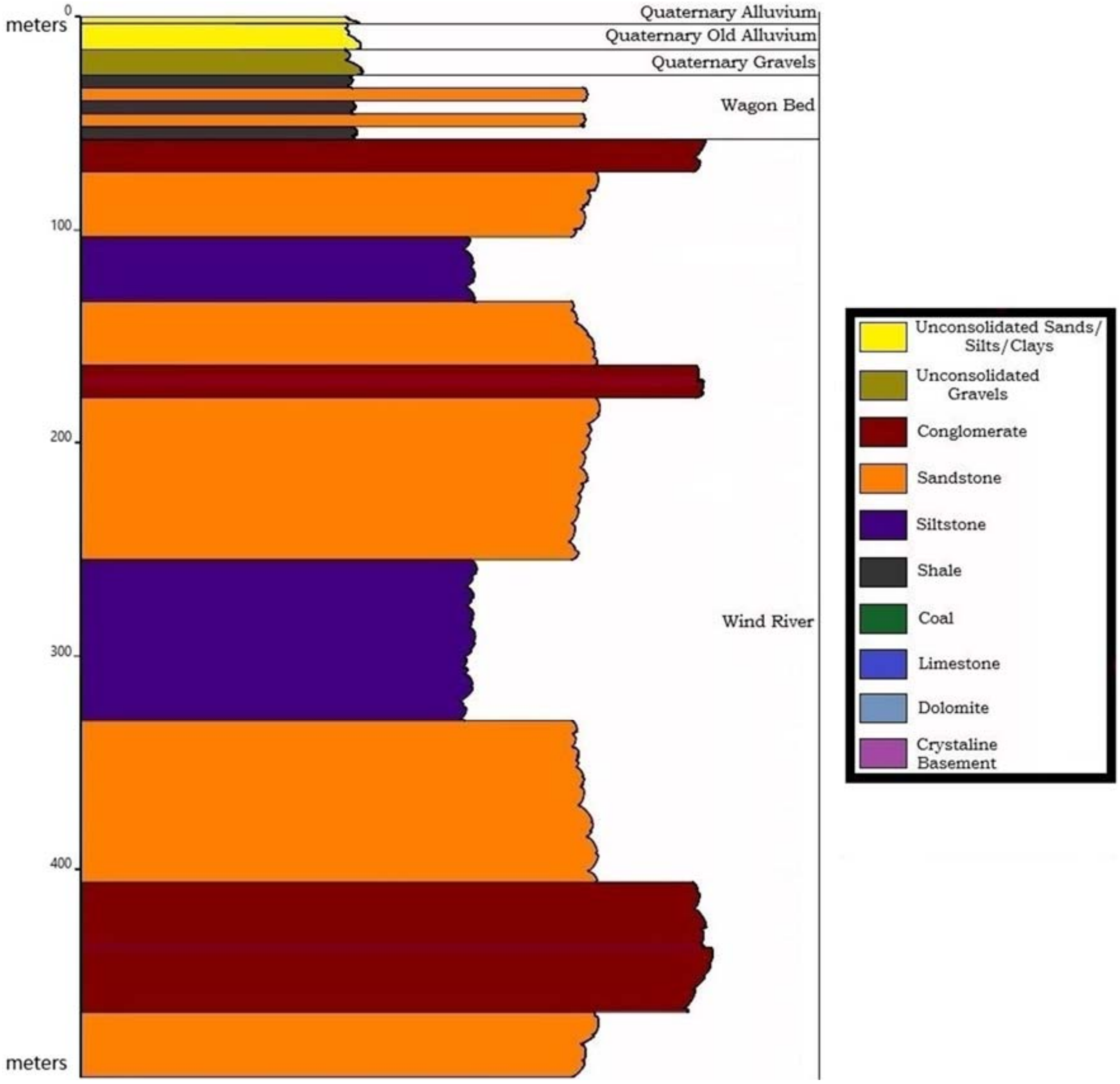

Figure 2-6. Continued from Figure 2-5. This is a closer look at the first 497 meters (1,630 feet) of stratigraphy at Birdseye Creek.

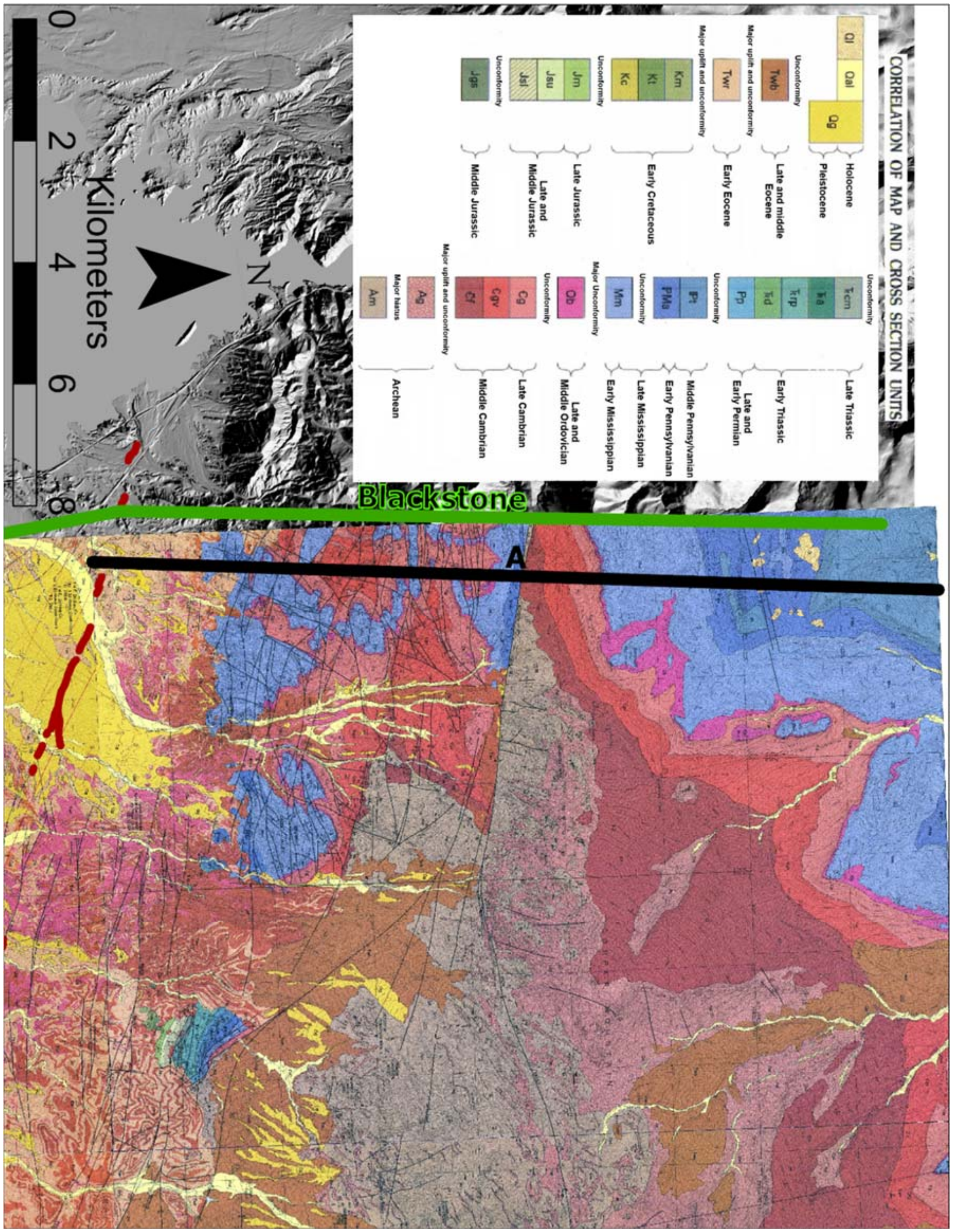

Figure 2-7A. Quadrangle map GQ-1537 (Thaden, 1980) and part of GQ-1439 (Thaden, 1978). This figures map centers on the line of section A-A’ from GQ-1537. The black and red lines on the map denote the line of section and the Stagner Creek Fault respectively. From the cross section (Figure 2-7B), point A is the southern end and A’ is the northern end of the line of section in the map.

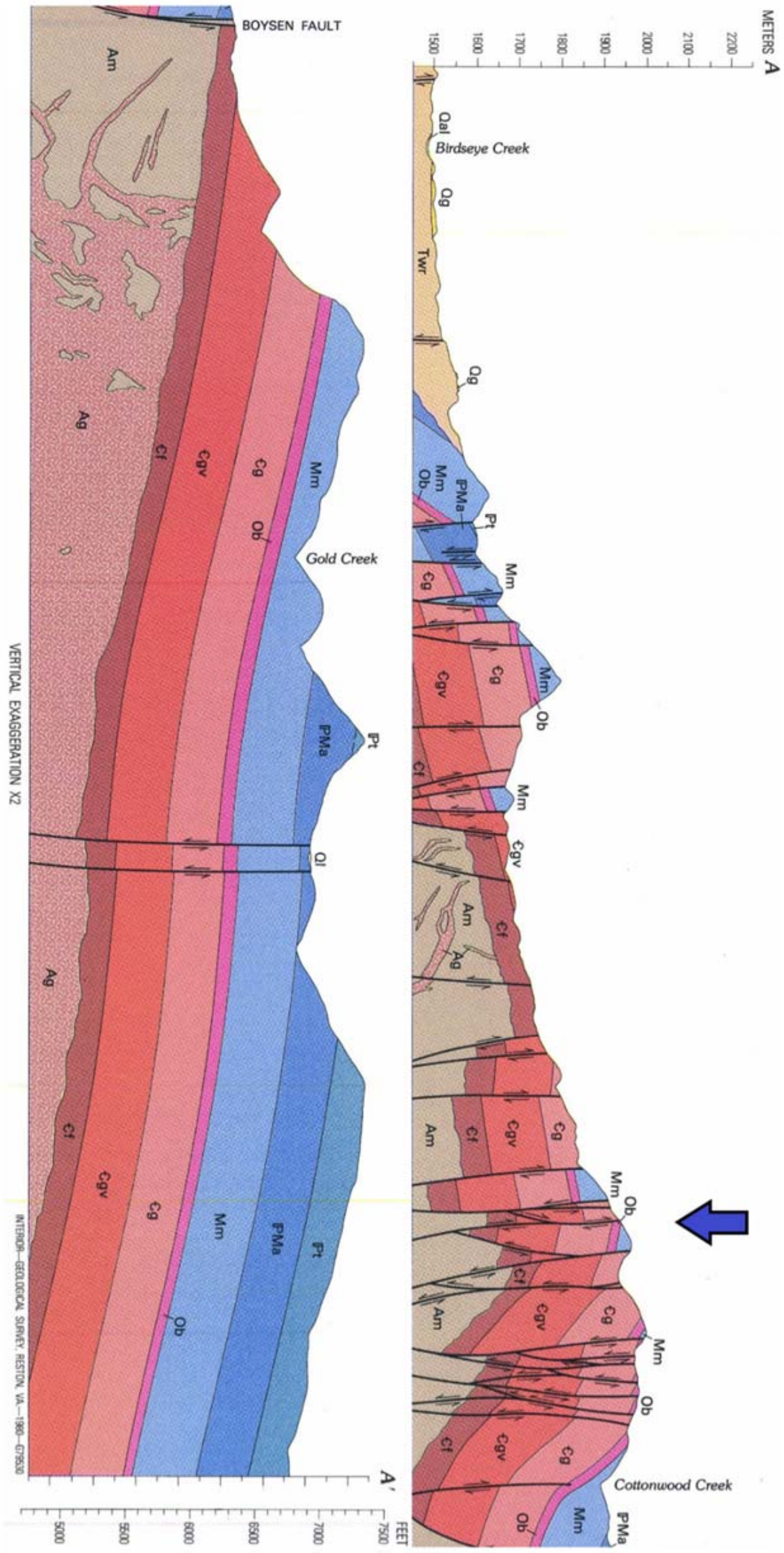

Figure 2-7B. Cross Section A from quadrangle map GQ-1537 (Thaden, 1980). The blue arrow in the cross section denotes the point of dip direction change. This shows the anticlinorium of the Owl Creek Mountains. The map can be seen in Figure 2-7A.

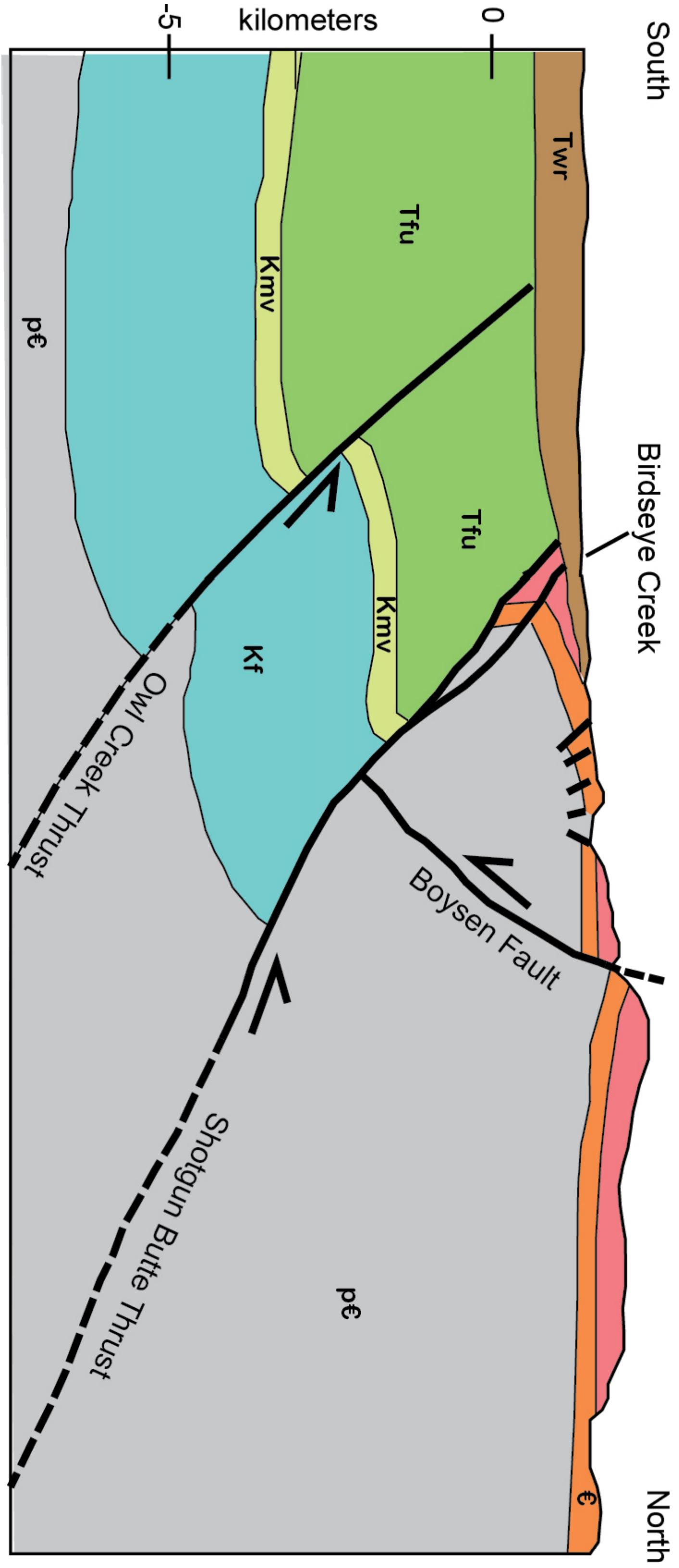

Figure 2-8. A rework of Cross Section 14 from Blackstone (1990). See the map in Figure 2-7A for the line of section.

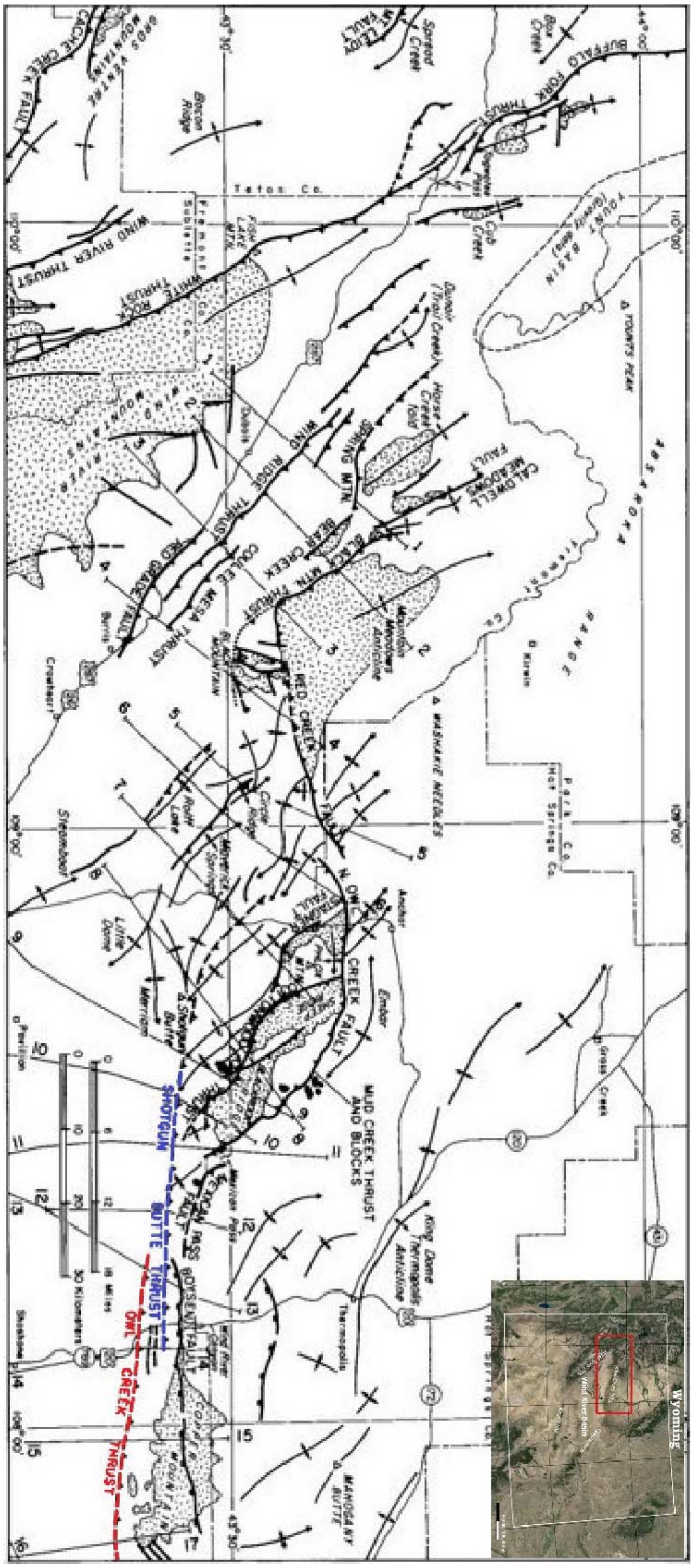

Figure 2-9. A map of deformation structures from Blackstone (1990).

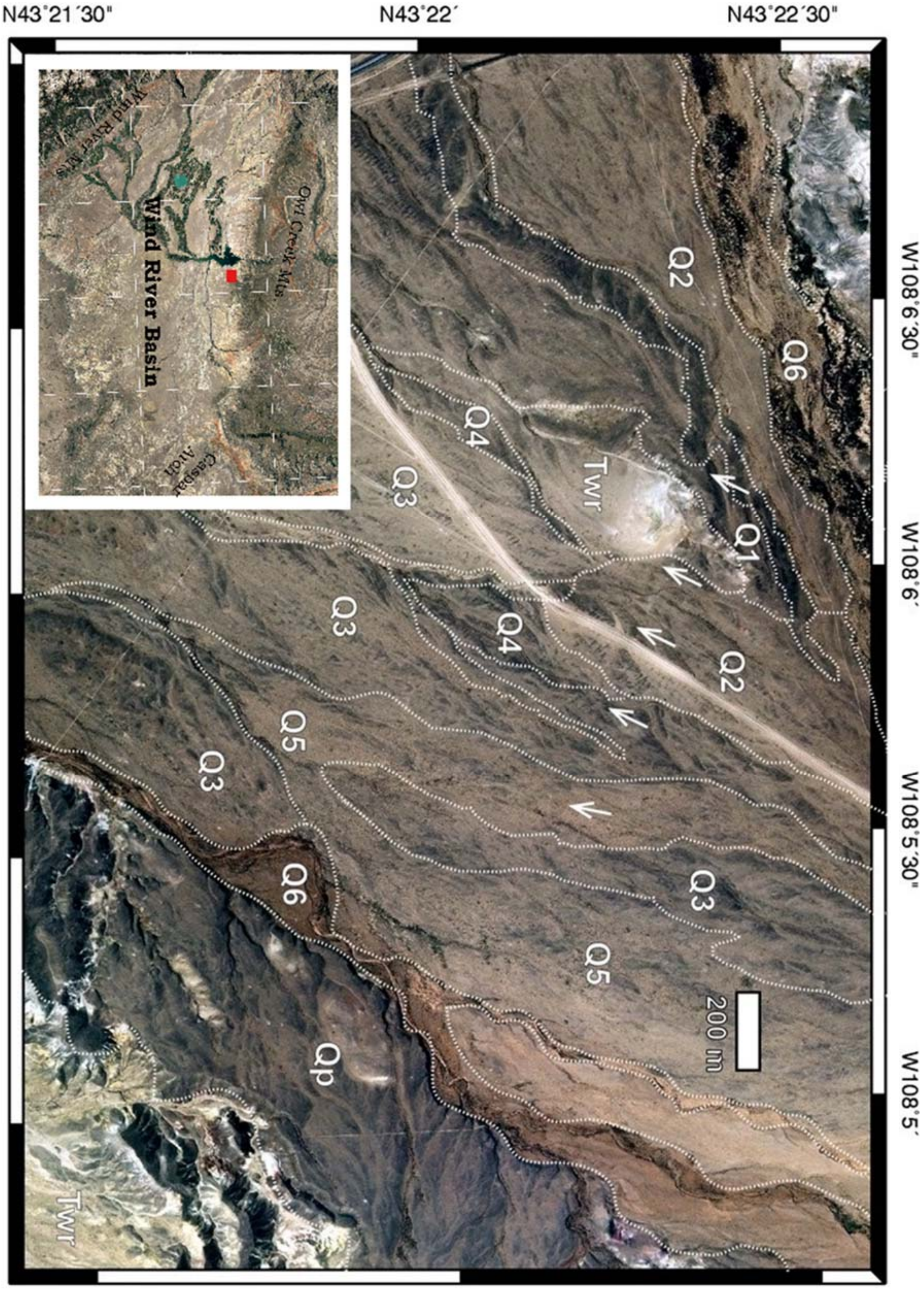

Figure 2-10. Divided gravel sections in the alluvial fan taken from DeLisle et al. (2016) and adapted from Geomatrix Consultants (1988). White arrows indicate the fault scarp.

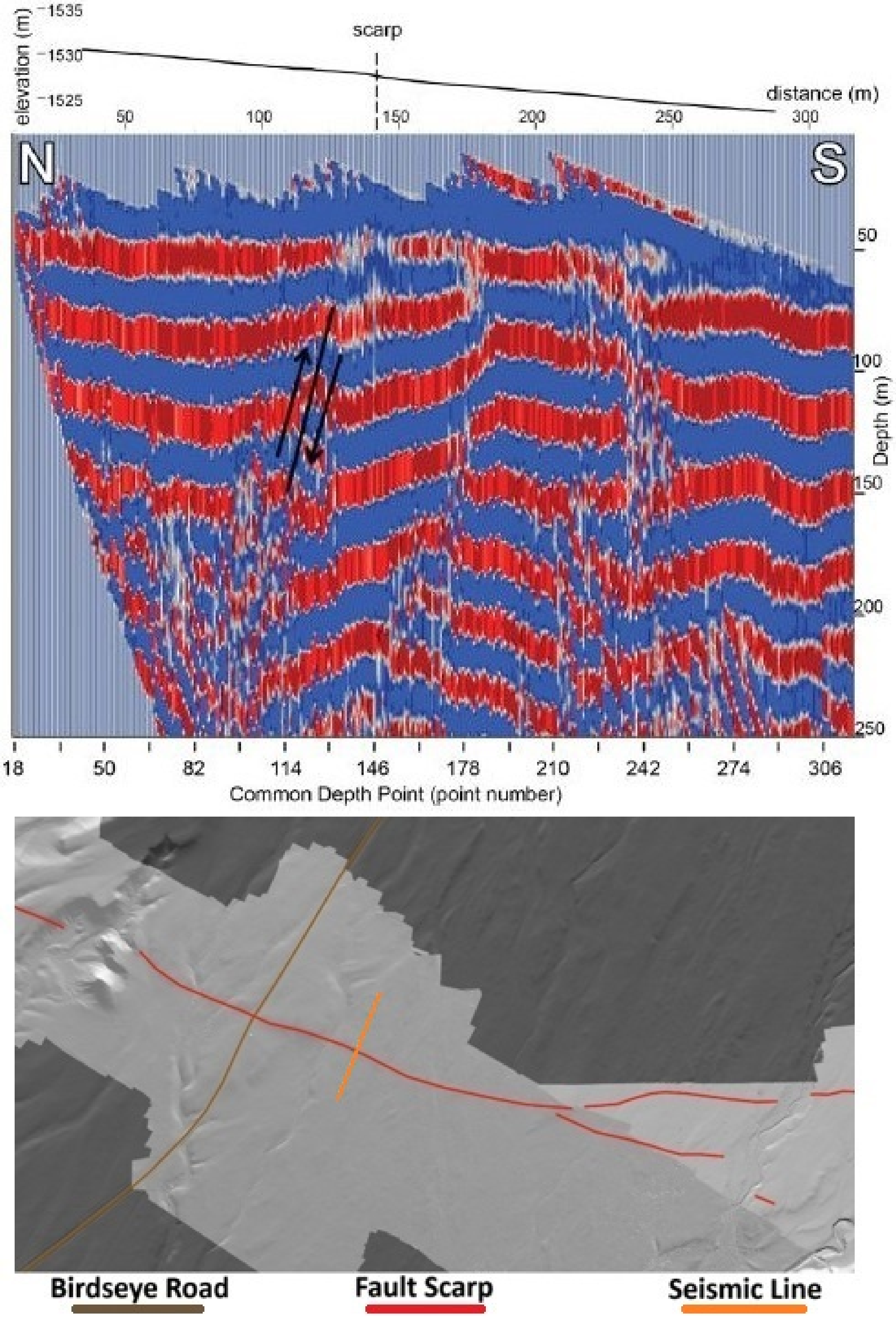

Figure 2-11. Shallow seismic reflection profile and seismic line across surface Q3. The profile was taken from Abousaif (2012). For a reference of location, refer to the intersection of the fault scarp with Birdseye Road in Figure 1-2.

Chapter 3: Neotectonic Geomorphology

Neotectonic geomorphology is the study of landforms over time and space in the very recent geologic past. Photogrammetry is an excellent tool for this and one that has been increasingly important in the last half century. Aerial photogrammetry has been employed in the use of DEM development. Using these DEMs in conjuncture with improvements in higher resolution imaging have allowed for the study of microtopography. This can show how certain parts of a single landform change in relation to parts adjacent to them. A great example of this is scarp evolution.

3.1 Methodology

DEM Development

When using a single aerial photograph, no aspect of depth, or in this case height, can be obtained. However, two photographs from slightly different angles called a stereo-pair can display this third dimension when using a stereoscope. A technique called structure from motion (SFM) greatly improves on this idea by using a group of photos. The technique recreates real world scenes from SFM algorithms based on the derived positions of the photographs in three-dimensional space with the product being a point cloud that is able to be georeferenced (Fonstad et al., 2012). By using these point clouds, a three-dimensional environment can be built from the photographs which can be used for a landscape's elevation model. Focusing on SFM, a higher resolution DEM than what is available publicly through the USGS will be created. This enables the creation of more precise elevation profiles across the fault scarp seen in Figure 1-2. Calculations for fault scarp degradation can then be done on the various gravel surfaces displayed in Figure 2-10 that the fault cuts across.

The development of the DEMs for use in this investigation was done using a small unmanned aircraft system (UAS) with a digital camera attached. A large number of photos were taken and then processed using Agisoft Metashape, (https://www.agisoft.com/) a software product designed to process digital images and from them, create 3D spatial data.

Data Collection

This study expands the spatial extent of a previously collected, drone-based photogrammetric survey (DeLisle et al., 2016). The prior survey only captured the trace of the fault in the immediate area of Birdseye Creek Road. A strategy was created to do two surveys, one on each of the west and east sides of the original 2016 survey to extend the data in the hopes of uncovering the trace of the fault in either direction.

Before each flight, a series of ground control points (GCPs) were placed within the field of view of the UAS's camera and then precisely located using Real Time Kinematic (RTK) Global Navigation Satellite System (GNSS; previously "GPS") measurements (Figure 3-1). A total of eight GCPs were placed and their locations recorded for each flight. During the flight of each survey, approximately 1,500 photos were taken along the UAS's flight path in such a manner that each photograph in sequence could be overlapped with the next in order to build a series of images that captured the entire area without gaps.

Data Processing

Aligning the photos was done in the Agisoft Metashape software by manually selecting the correct position of the GCPs in each photograph they appear in. These GCPs are reference points the program uses to correct for error when creating the point cloud. The more photos that have these reference points, the more accurate the point cloud will be. When completed, the eastern survey's point cloud contained nearly 170 million points and the western totaled about 121 million points.

Once the point clouds were completed, they were exported as LAS files so that they can be imported into Cloud Compare (https://cloudcompare-org.danielgm.net/), a software that is capable of separating ground points from non-ground points. Within cloud compare, two methods were attempted at separating vegetation points from ground points. The first method involved using the plugin tool called the Cloth Simulation Filter (CSF). To give an idea what this tool does, it simulates flipping the point cloud upside down and draping a cloth overtop of the underside. Ground points are considered where the cloth rests in a flat position and non-ground points are considered where the cloth would sag. The "tightness" of the cloth can be adjusted through the CSF settings. The second method involves a tool called 3DMASC. This plugin uses multiple attributes, scales, and clouds by computing descriptive features of the chosen point clouds before training a model to predict point classes. The user is able to define the descriptive features to use, the point clouds to process, and the classes to target (Plateforme LIDAR, 2024). Between the two methods, the CSF filter was the more simplistic and quicker of the two, but it produced less than satisfactory results for what was needed. 3DMASC was much more involved and the processing time was significantly longer, but the results were far improved over the CSF filter in removing non-ground points. As such, it was decided that using 3DMASC for building the DEMs for use with fault scarp degradation was the way to go. A 25cm resolution was completed for all processed DEMs when rasterized through Cloud Compare.

Fault Scarp Profile Development

A scarp is defined as a steep embankment or sudden change in elevation relative to the area around it. In the case of a fault scarp, it is simply a visible lineation with elevation change that separates the upper and lower original surfaces (Wallace, 1977). With all scarps, fault scarps included, the degradation process initiates after formation. The morphological change in shape of fault scarps brought on by the degradation process is what needs to be observed. Degradation increases with time meaning the principal slope angle decreases as time progresses (Wallace, 1977).

Data Collection

With the rasterized DEMs overlaid on the field site's map, a series of profiles across the fault scarp were selected to show the offsets on the various gravel surfaces seen in Figure 2-10. Once the profiles were finalized, the coordinates of their endpoints were then obtained and used in a program called pyScarpFit (Polun, 2021) to both display the profile's image and produce statistics of the scarp.

Data Processing

The idea behind a fault scarp profile is to capture a plot of maximum scarp slope versus scarp offset by taking a profile that is parallel to the strike of the scarp (Hanks et al, 1984). In doing so, it is possible to estimate an age of a fault scarp using the Hirano's equation (3.1):

$$\frac{\partial u}{\partial t} - \kappa \frac{\partial^2 u}{\partial x^2} = 0$$

where κ is the diffusivity constant, t is time, h is height of the scarp, and x is the horizontal distance. Two solutions to this equation are found in Hanks et al. (1984) and Hanks (2000). Equation 3.2 assumes a single uplift event

$$u(x,t) = a\, erf\left(\frac{x}{2\sqrt{\kappa t}}\right) + bx$$

where equation 3.3 assumes a multi uplift event, otherwise known as a steady-state event

$$u(x,t) = (a + At)\, erf\left(\frac{x}{2\sqrt{\kappa t}}\right) + \frac{Ax^2}{2\kappa}\left[erf\left(\frac{x}{2\sqrt{\kappa t}}\right) - sgn(x)\right] + \left(\frac{A_x}{\kappa}\sqrt{\frac{\kappa t}{\pi}}\right) e^{\left(\frac{-x^2}{4\kappa t}\right)}$$
$$+ bx$$

These were used for generating the scarp profiles in Python (https://github.com/seanpolun/pyScarpFit). Diffusion parameters are solved by a grid search, which identifies the midpoint of the scarp (defined as x = 0), the upper and lower far field slope, and the vertical offset of the scarp (Potter, 2022).

3.2 Neotectonic Geomorphology Results

The 3DMASC tool has greatly improved on eliminating non-ground points from the DEMs. Using the western section in Figure 3-2 as an example, you can clearly see gaps in the DEM where large amounts of vegetation exist. This causes holes in the DEM model. We know that these areas would likely cause problems for our scarp profiles, so when choosing the profile sections, highly vegetated areas were avoided. Fortunately, these areas were mainly confined to the areas of active alluvium where the scarp was nonexistent anyway. For aesthetic purposes, the USGS 1 meter DEM in Figure 3-2 fills the gaps in the UAS 25cm DEM. This has no bearing on the scarp profiles.

Looking at the profiles, and specifically the heights of the scarps, we see a decrease in height of the scarp going from older to younger surfaces. This suggests that older surfaces experienced a greater number of faulting events than the younger surfaces. There is no profile for surface Q6 as we do not see any deformation on any of the Q6 surfaces. This agrees with the Geomatrix report. However, we do see a minor raised element in the Q5 surface as can be seen in profile Q5 of Figure 3-5. This disagrees with the Geomatrix report but is clearly visible in the profile.

An additional scarp profile was made in a surface that was unlabeled in the Geomatrix report. This profile is labeled as profile Q? in both Figure 3-2 and 3-5. The scarp height is calculated as 0.70m by the pyScarpFit program. It is slightly lower, but comparable to profile Q3's scarp height of 0.88m. This suggests that the unlabeled surface is most likely a Q3 surface with an age 15-40 ka and comparable to Pinedale age soils.

Table 3-1 summarizes the results of the scarp heights and compares them to the Geomatrix report's results. The height values for this investigation are similar to the ones found in the report for surfaces Q1, Q3, and Q4 but disagree with surface Q2. Their measurement for Q2 is nearly 1 meter greater than what was found in this investigation. For the unknown surface, the calculation for the rate was made by using the relative time of the Q3 surface suggested in the Geomatrix report as this scarp height was closest to the known height of the unknown surface. The rates found for it were consistent with the other surfaces. The only egregious outlier in the table is that of surface Q5's minimum rate 0.36 mm/yr. It appears much larger than the other, but after considering the relative ages listed for Q5 from the Geomatrix report, the scarp age is most likely closer to 7,000 rather than 1,000 years. Looking at the maximum displacement, all values lie between 0.04 and 0.06 mm/yr with 5 different surfaces measured that had relative ages set to them. The Geomatrix report had only 3, but their values were also consistent between 0.06 and 0.07 mm/yr.

Earthquake magnitude should correlate with the amount of displacement along the causative fault (Wells and Coppersmith, 1994). As such, calculating a magnitude for the displacement in the Q5 surface should be possible if the displacement across Q5 is assumed to be of a single event. From Figure 3-5, a displacement of 0.36 meters was measured. Using the moment magnitude versus maximum displacement graph in Figure 3-6, a magnitude 6.3 earthquake is found to be responsible for the displacement in surface Q5. With the displacement measurements in surfaces Q4 and Q5 being similar, it is suspected that the events that deformed both surfaces are identical meaning there is no event that isolates Q4 from Q5. Using Q5's displacement, we can extrapolate the number of events that occurred on the higher surfaces. These calculations are shown in Table 3-1.

The USGS 1m DEM has allowed for the identification of a lineation on the west side of Birdseye Creek opposite of the known fault trace of the Stagner Creek Fault in Figure 3-3. This is an important piece of evidence as it confirms the continuation of the fault toward the northwest. The trajectory of the recently found lineation is nearly identical to that of the known fault trace. If traced toward each other, they form parallel lines rather than forming a single line. This indicates that there is a step in the fault that isn't visible at the surface due to it being buried. Towards the southeast in Figure 3-4, the fault trace continues toward and across a separate deposit of the Q6 active alluvium. While not as well defined as in Figure 3-3, the trace of the fault is accentuated by exaggerating the height factor, or z factor, as well as altering the direction and angle of the sun's light. The z factor is increased to 8 times the normal and the light direction/angle is from the north at 45 degrees.

Chapter 3 Figures

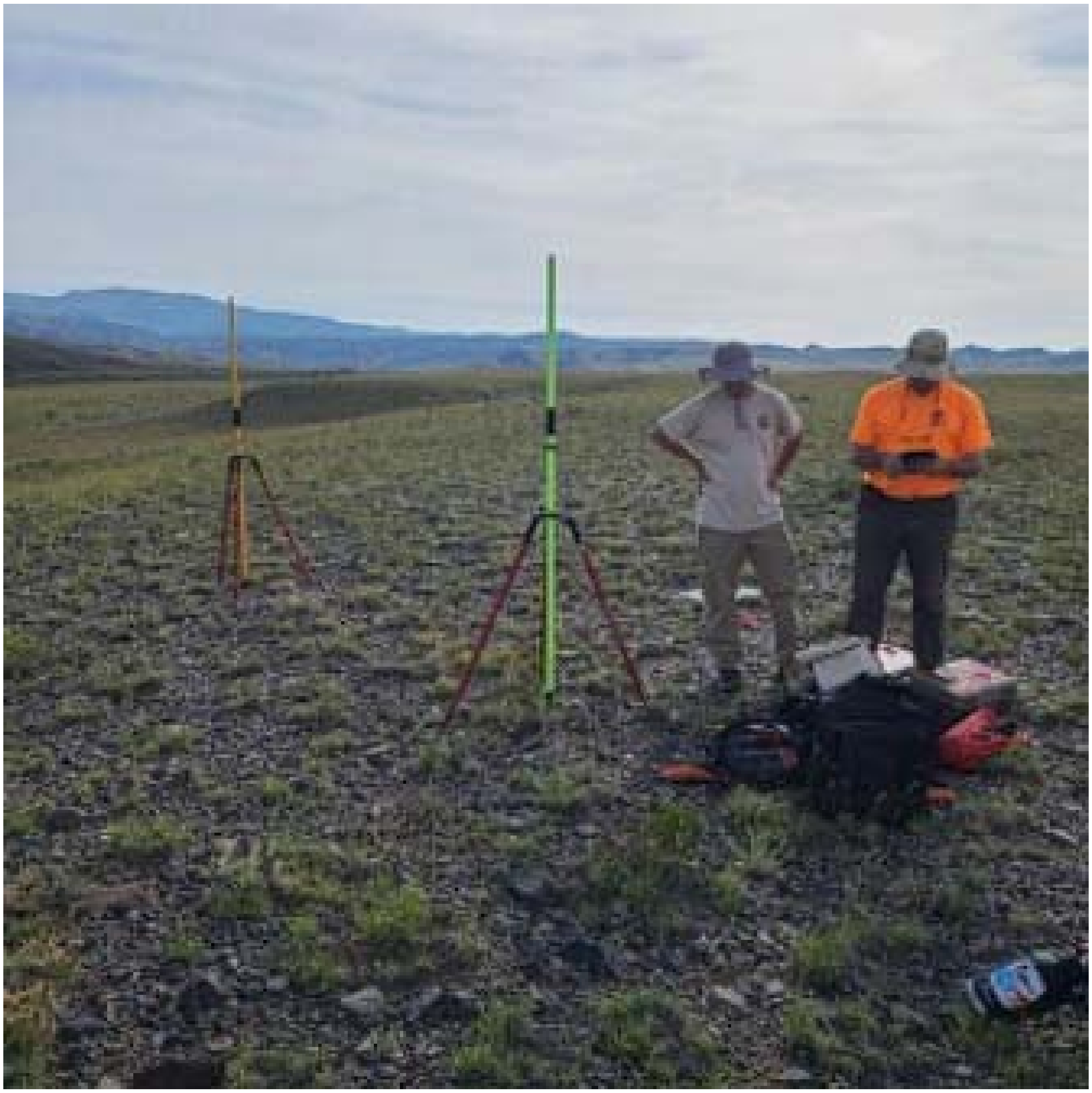

Figure 3-1. Photograph of setting up the RTK station.

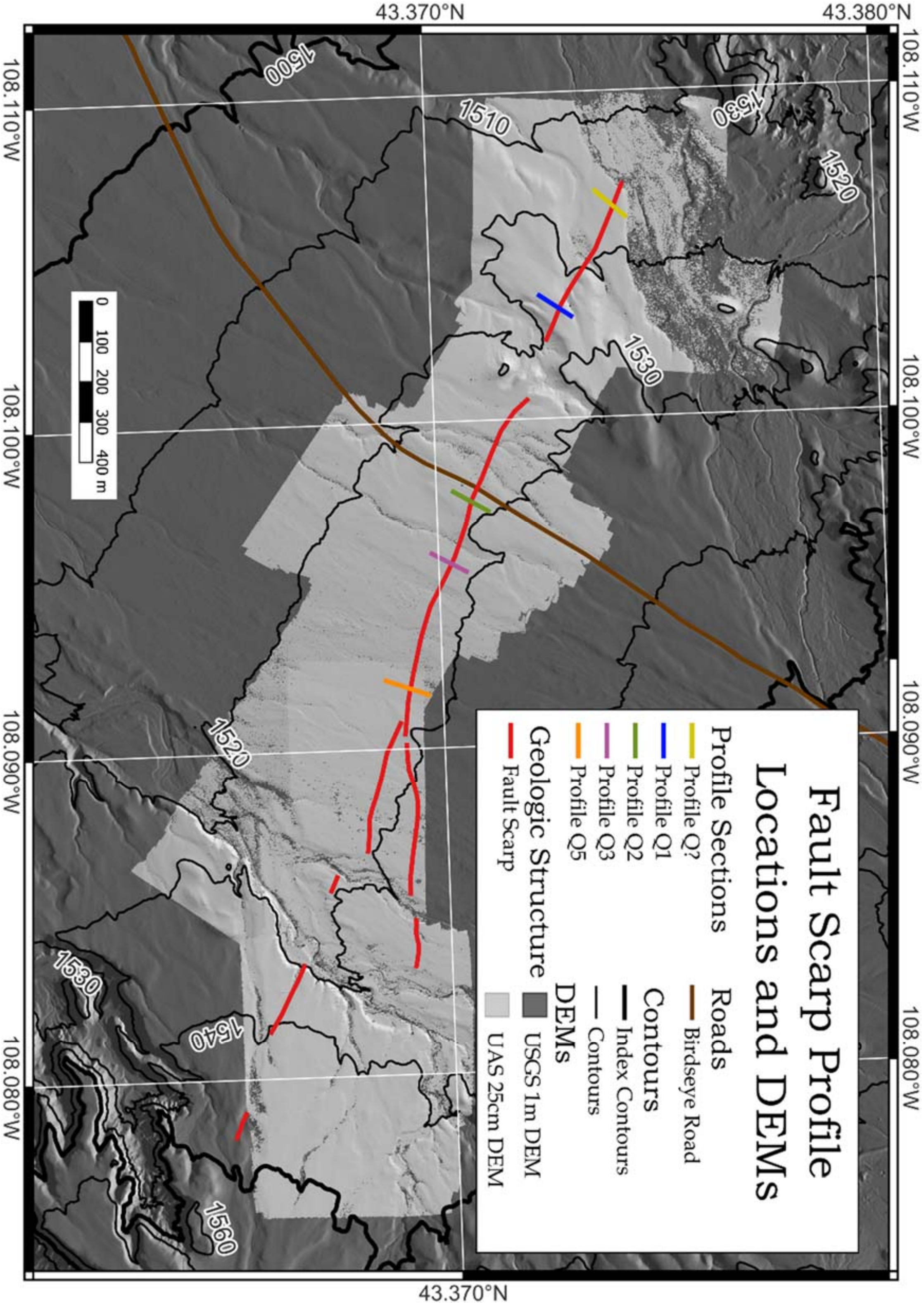

Figure 3-2. These are the locations of the five profiles selected across the Stagner Creek fault scarp. The labeling of each profile corresponds to the gravel surface that the profile path exists in. Gravel surface labels designated in Geomatrix Consultants (1988).

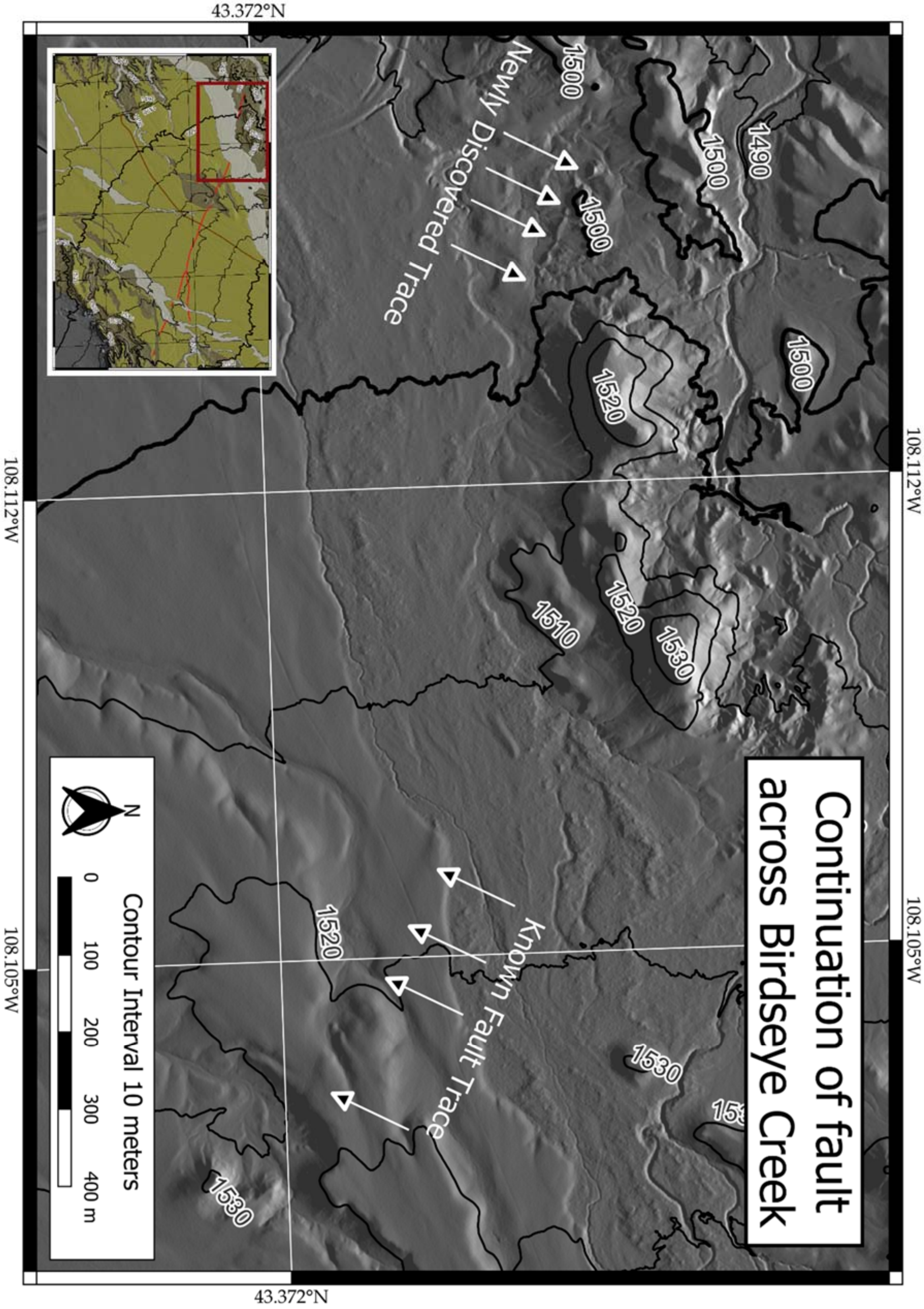

Figure 3-3. Map showing a newly found trace of the Stagner Creek Fault. Inset map from Figure 1-2.

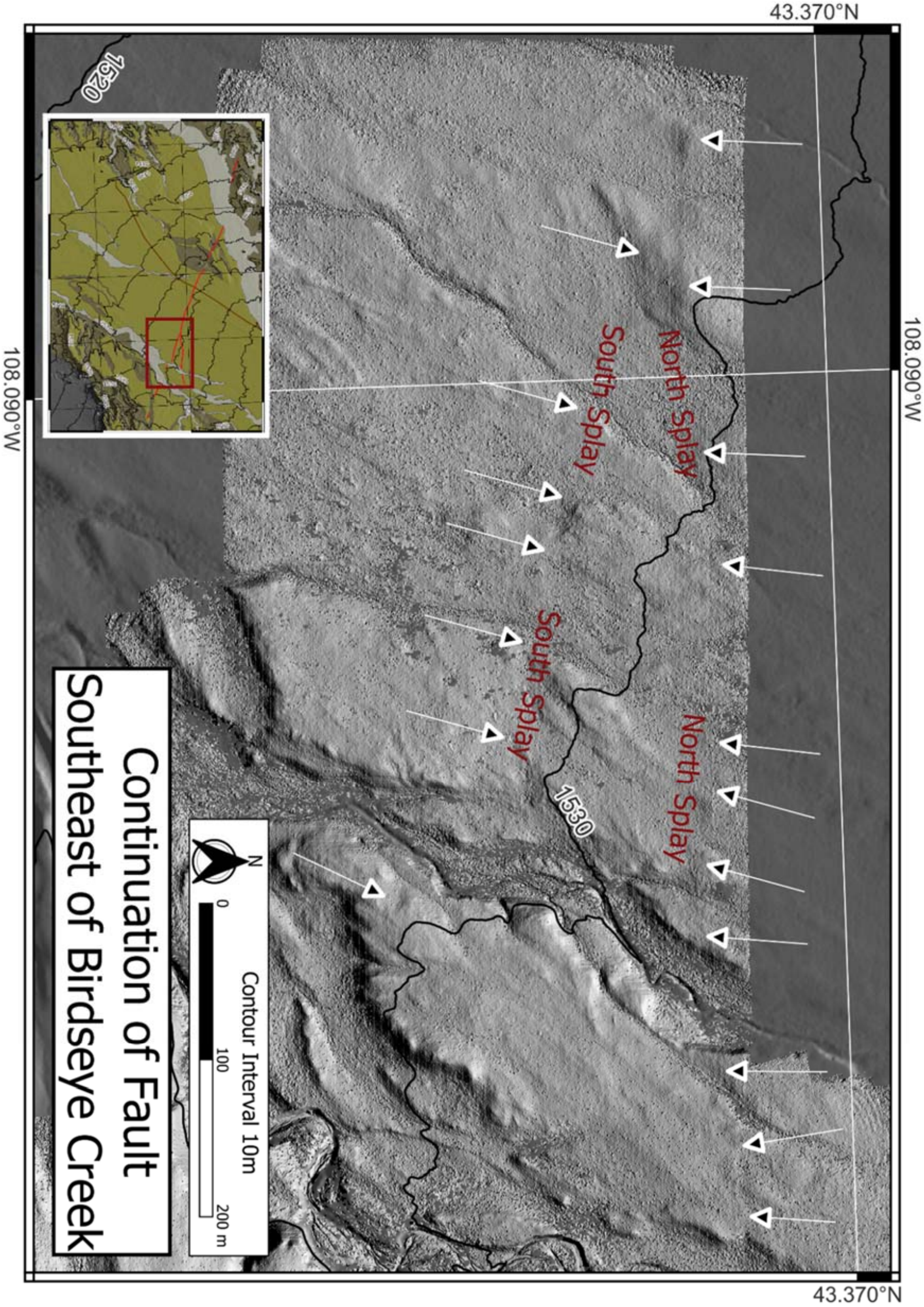

Figure 3-4. Map showing continuation of the Stagner Creek Fault southeast of Birdseye Creek. Inset map from Figure 1-2. DEM Z-factor exaggeration X8 and lighting angle due north.

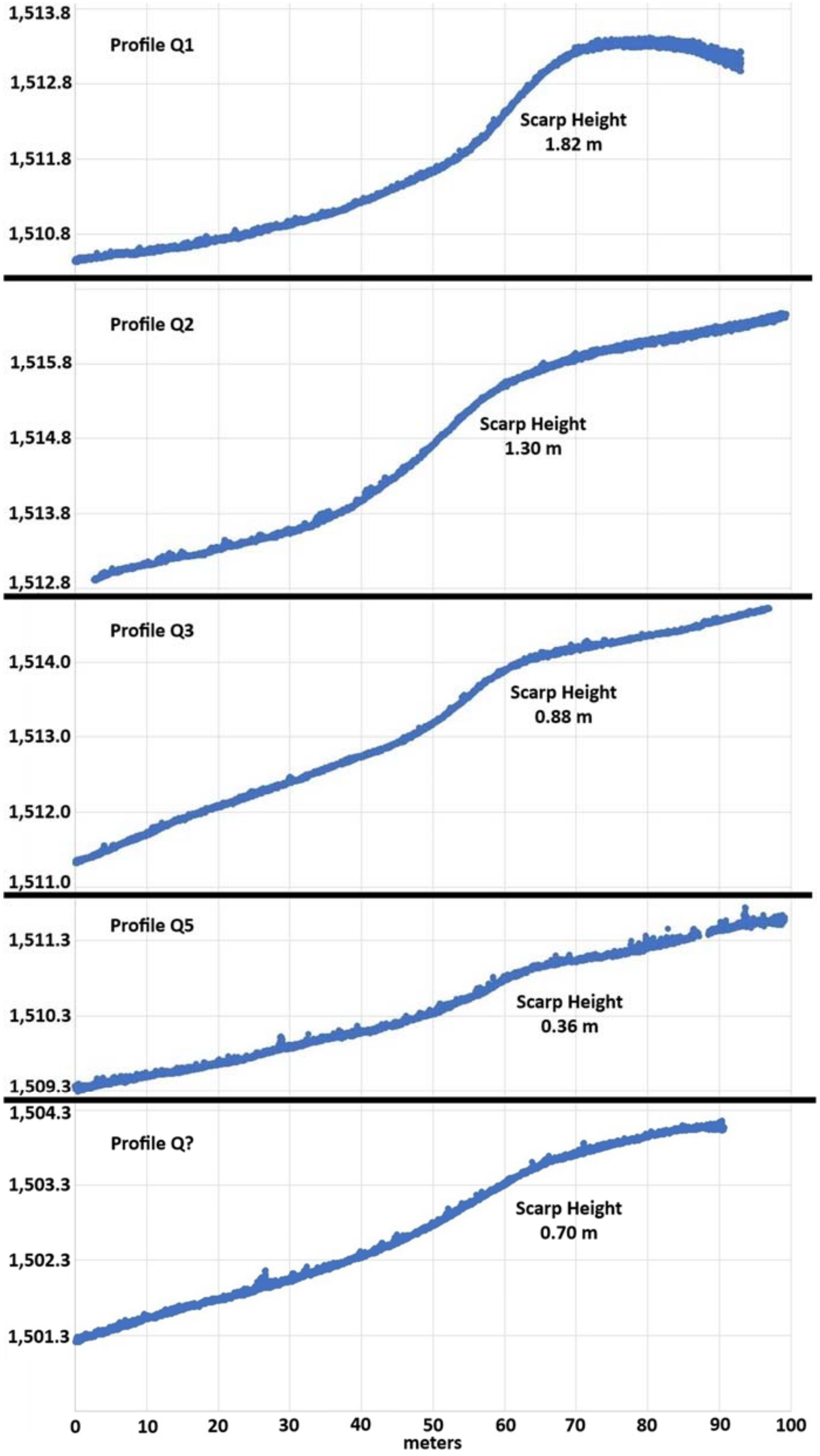

Figure 3-5. These are the fault scarp profiles from the map in Figure 3-2. The labeling of each profile corresponds to the gravel surface that the profile path exists in. Gravel

surface labels designated by Geomatrix Consultants (1988). Vertical Exaggeration is 10x in all profiles.

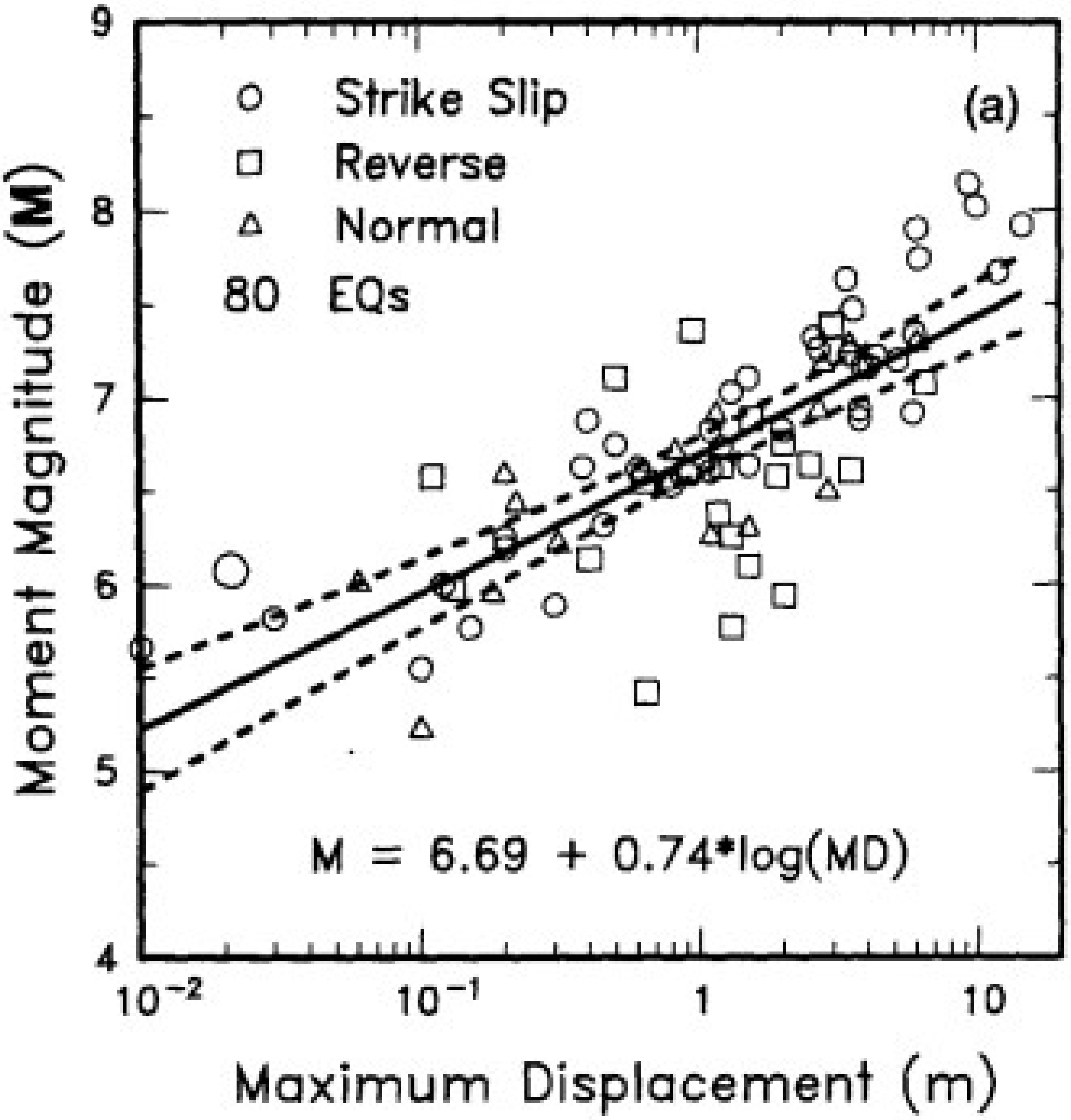

Figure 3-6. This is a scatter plot of Magnitude (M) vs Max Displacement with the displacement values on a logarithmic scale. The solid black line indicates line of regression that best fits the data where the dashed lines indicate 95% confidence interval. Figure and caption information taken from Wells and Coppersmith (1994).

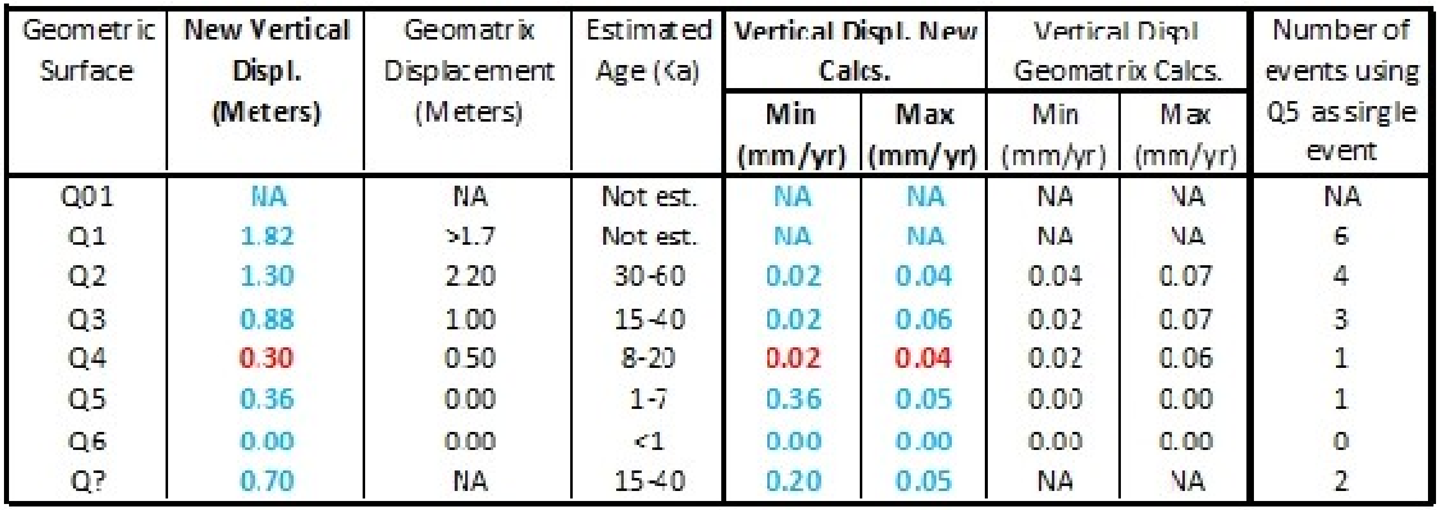

Geometric Surface	New Vertical Displ. (Meters)	Geomatrix Displacement (Meters)	Estimated Age (Ka)	Vertical Displ. New Calcs.		Vertical Displ Geomatrix Calcs.		Number of events using Q5 as single event
				Min (mm/yr)	Max (mm/yr)	Min (mm/yr)	Max (mm/yr)	
Q01	NA	NA	Not est.	NA	NA	NA	NA	NA
Q1	1.82	>1.7	Not est.	NA	NA	NA	NA	6
Q2	1.30	2.20	30-60	0.02	0.04	0.04	0.07	4
Q3	0.88	1.00	15-40	0.02	0.06	0.02	0.07	3
Q4	0.30	0.50	8-20	0.02	0.04	0.02	0.06	1
Q5	0.36	0.00	1-7	0.36	0.05	0.00	0.00	1
Q6	0.00	0.00	<1	0.00	0.00	0.00	0.00	0
Q?	0.70	NA	15-40	0.20	0.05	NA	NA	2

Table 3-1. Comparison of Geomatrix results and results from this investigation. The blue text represents this investigation’s measurements and calculations. The red text for Q4 indicates the measurement was taken from Gomez et al (2016) and used for the new calculations for that surface.

Chapter 4: Relative Age Dating

Relative age dating is the science of time relations. For the field site at Birdseye Creek, the goal is to relate various Quaternary surfaces to each other in this way. Soil sampling is a common practice for this, but the report by Geomatrix Consultants shows tests done with this method already. Finding a different method to compare to the Geomatrix report's soil technique would be ideal. Elevation heights between surfaces is dependable when dealing with stream incision, but heavily dissected surfaces or surfaces across significant distances can prove difficult to quantify.

4.1Methodology

Rock strength is a factor that is dependent on time. The outer surface of rock is exposed to natural agents of weathering such as air, water, and sunlight. As exposure time for rock increases, there should be a corresponding decrease in the strength of a rock's surface. In order to test this, an inexpensive tool called a Schmidt Hammer was employed as it is capable of collecting large amounts of data on materials that can show high variability (Goudie, 2016). The number of samples, size of samples, strikes per sample, strike method, type of material, and number of operators are factors that will need to be considered while testing.

The number of samples for a Schmidt Hammer study is significant when analyzing results. If sample size is insufficient, misrepresentation of data could occur. As some materials are more consistent than others, material type can be a factor when deciding the number of samples Niedzielski (2009). suggests 33 as the minimum number of samples for basaltic material in order to get a mean rock strength value that is statistically correct.

For sample size, the rocks being tested are recommended to be rectangular shaped with at least 100mm of thickness. Any thinner than this and the rock becomes susceptible to vibration and fracturing (Matthews and Winkler, 2022). The surface area of the sample is also significant as it needs to contain enough space across the surface to allow for numerous strikes from the Schmidt Hammer.

The number of strikes per sample is equally important as the number of samples in a study. Variability between samples can be high in strong materials (Niedzielski, 2009) so it is important to have both large amounts of samples as well as strikes per sample when doing Schmidt Hammer analysis.

Single and double strike methods have been done using the Schmidt Hammer. The single strike method gives an R-value (rebound-value) reading that would need to be compared with known values of the material being tested. With two strikes in the same location, both a weathered and non-weathered strength value can be obtained. Using multiple strikes on a sample has determined that the greatest difference between any two consecutive strikes occurs between the first and second strike (Poole and Farmer, 1980), so any more than two strikes in the same location will only yield diminishing results. In the double strike method, the first strike measures the weathered strength of the rock and the second strike measures the strength of the rock that represents a freshly exposed surface. This difference can be used as a proxy for relative time of exposure to weathering agents when comparing multiple weathered surfaces.

Since we are using the double strike method to find both a weathered and non-weathered strength value in the selected samples, the type of material being tested is vital.

The material must be one where it remains unaltered below the surface. This eliminates most sedimentary rock, as weathering agents are able to penetrate them due to their porosity. Course rock types could present a problem if various minerals crystalize. This will cause samples to be disproportionate in strength across their surface. A basaltic type rock would be the ideal material type as it is non-porous and aphanitic. Fortunately, this material type is found in both large size and abundance across many of the Quaternary surfaces at the Birdseye Creek field site. An example of one of the samples tested is visible in Figure 4-1.

The Schmidt Hammer is simple to use, but difficult to be consistent with. Sampling with multiple operators could produce inconsistent data. Results from Viles, 2011 concluded that operator variance with the classic Schmidt Hammer as well as other instruments designed to measure rock strength needs to be considered in geomorphological studies. The best way around this problem would be to use a single operator for all samples tested.

The report by Geomatrix Consultants (1988) contains a map (adapted to by DeLisle et al, 2016) of the intersection of the Stagner Creek Fault and Birdseye Creek that has divided the alluvial fan into sections labeled Q1-Q6 and classified them based on their relative elevation to each other as well as comparing the soils to similar soils of the Bull Lake and Pinedale glaciations. These divisions in the map between different gravel surfaces of the alluvial fan are ideal for testing the surfaces of weathered rock for strength and comparing the data to see if a correlation can be made. An additional surface labeled Q01 will also be tested which is just north of the Q1-Q6 sites. This surface is at an elevation of about 60-70m higher and can be seen in Figure 4-2. If the data trends as suspected, this additional surface should be expected to have higher average values than any of the Q1-Q6 surfaces as it is higher in elevation and therefore the exposure time is greater.

Data Collection

A total of 7 surfaces were looked over for possible samples to be tested on with the Schmidt Hammer. Surfaces Q01, and Q1-Q3 contained more than enough samples to get a reasonable amount of data. Surface Q4 was sparse in samples but still contained enough to collect data on. Surfaces Q5 and Q6 lacked large enough samples to be tested in accordance with the suggested size of 100mm of thickness (Matthews and Winkler, 2022). Niedzielski (2009) suggests a minimum quantity of test samples for basaltic type rock to be 33 to get a statistically correct average. The quantity of samples here totaled 56, with at least 10 on each surface except surface Q3 which only has 5 samples tested. Preferably, the total for each surface should be closer to the quantity of 33, but time constraints and quantity of available samples for the younger surfaces proved to be a limiting factor. To counter this, each sample was struck no less than 10 times so that an appropriate average R-value for each rock was obtained. A total of 600 pieces of data were recorded over the 6 surfaces that had rocks large enough for sampling. This means that since the method of hammer usage required two strikes for each piece of data, a total of no less than 1,200 strikes with the Schmidt Hammer were taken. This does not account for bad strikes that were not recorded. To avoid operator variance, one operator collected all data with a second individual used as a spotter.

Data Processing

The data was compiled into a spreadsheet where each sample's tests were held against a standard deviation of 2. For each sample, if the standard deviation rose above 2, the top/bottom 10% of the data for that specific sample was culled to remove outliers. After this was done, the following equation (4.1) was used to calculate a contribution to the weighted average of each sample's corresponding surface:

$$\left[\frac{1}{n}\sum_{i=1}^{n}(s_2 - s_1)\right] \times \left[\frac{1}{\sigma^2}\right] = C$$

where n is the number of tests on the sample, s_1 is the first strike, s_2 is the second strike, σ is the standard deviation, and *C* is the contribution. Once the contribution for each sample is calculated for a given surface, a second equation (4.2) was employed to finalize the weighted average:

$$\frac{\sum_{i=1}^{x} C_i}{\sum_{i=1}^{x} W_i} = w_{avg}$$

where *x* is the number of samples, *C* is the contribution, *W* is the weight, and w_{avg} is the weighted average for the given surface.

4.2 Relative Age Dating Results

Figure 4-3 is a graph of data from the Schmidt Hammer tests. It gives the weighted average differences of each surface denoted be the red dot and error bars denoted by the top and bottom of the yellow boxes. The weighted averages show a downward trending R-value in the older surfaces of Q01, Q1, and Q2, which is what was expected. The trend changes in the younger surfaces, leveling off as surfaces Q2, Q3, and Q4 show near similar values. This was not expected. Since we are seeing similar values in these three surfaces, it is suspected that significant exposure time differences are not present between these surfaces to distinguish between them using the Schmidt hammer. The limited sampling of Q3 may explain why the error bars for this surface have a much larger range, the total data may be insufficient in accordance with Niedzielski (2009). With more samples, it is expected that this error bar would lessen while the weighted average would change very little.

Surface Q01 does not lie on the fault scarp like the other sampled surfaces. The significant height difference between it and the other surfaces was used to test that higher surfaces represent more exposure time, and therefore are older. The value in Figure 4-3 for surface Q01 supports this.

The unknown surface Q? is also represented here. The chart shows that in the relationship between all Quaternary surfaces tested, average R-values for Q? correlate between surfaces Q1 and Q2. This is not what was expected, but its close positioning to Q1 versus Q3 on the map in Figure 4-4 could be a factor skewing the data toward Q1 values. Debris from the Q1 surface could have shed onto Q3 at some point. This is only speculation as more sample testing would be needed to confirm.

In all, there is a definite correlation between exposure time and relative elevation. The downward trend of the data, specifically for the older surfaces, match that of the soil age testing in the Geomatrix report. The younger surfaces do not express this downward trend individually, but could be lumped together to describe a range of younger surfaces relative to the older Q01 and Q1 surfaces.

Chapter 4 Figures

Figure 4-1. One of the many samples tested with the Schmidt Hammer.

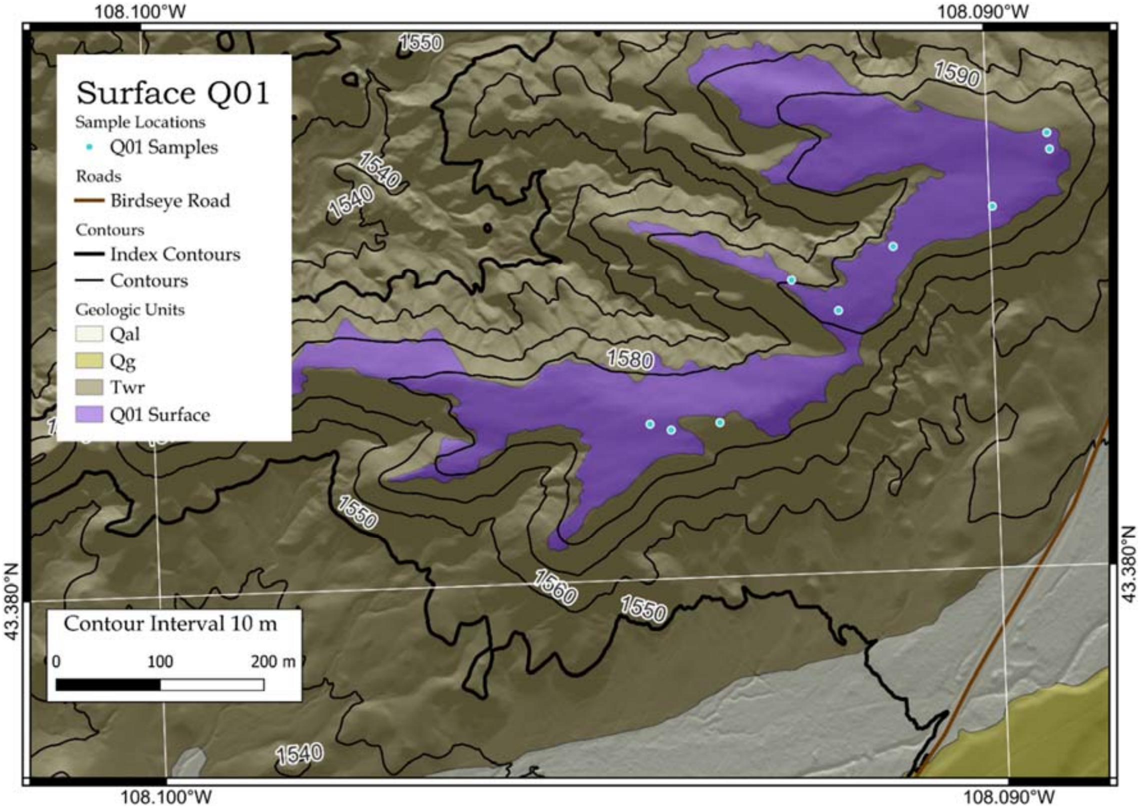

Figure 4-2. Map of surface Q01, a specific Qg surface identified for Schmidt Hammer sampling.

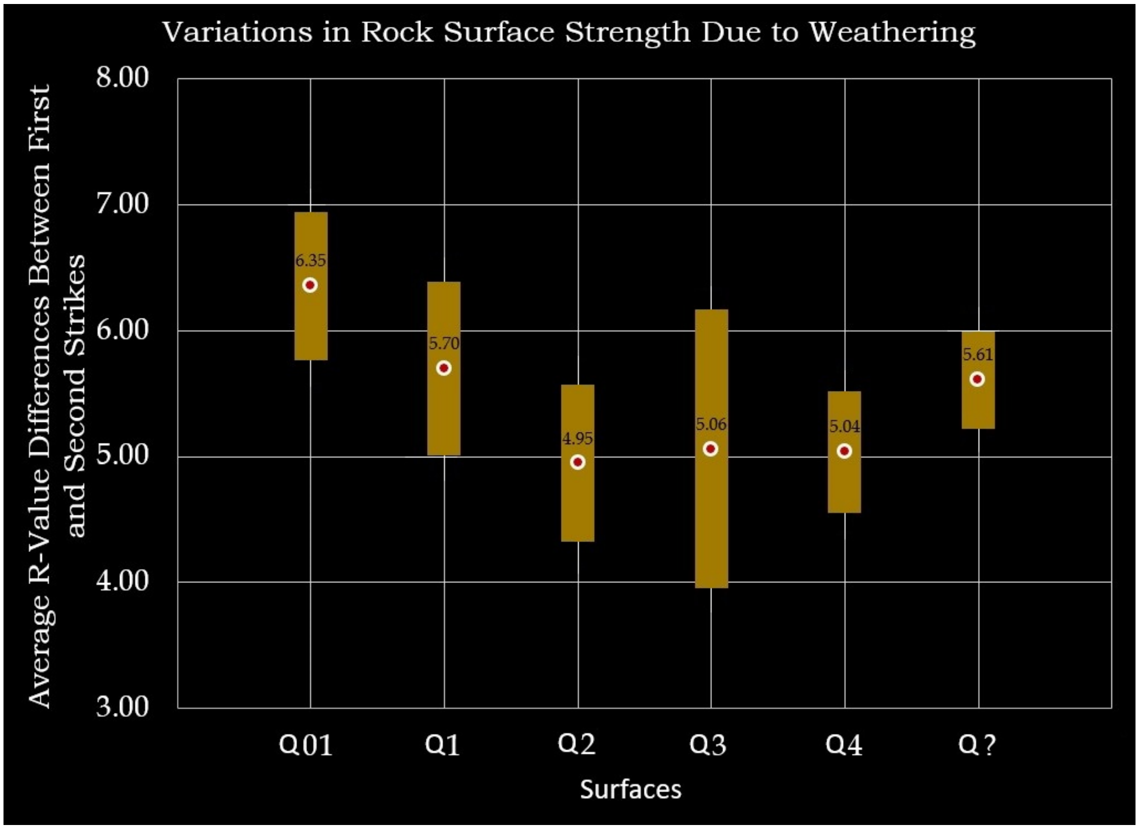

Figure 4-3. Results of Schmidt Hammer sampling. The upper and lower extents of each box represent the upper and lower quartiles of each surface's data respectively. The red dot represents the mean value for each surface respectively.

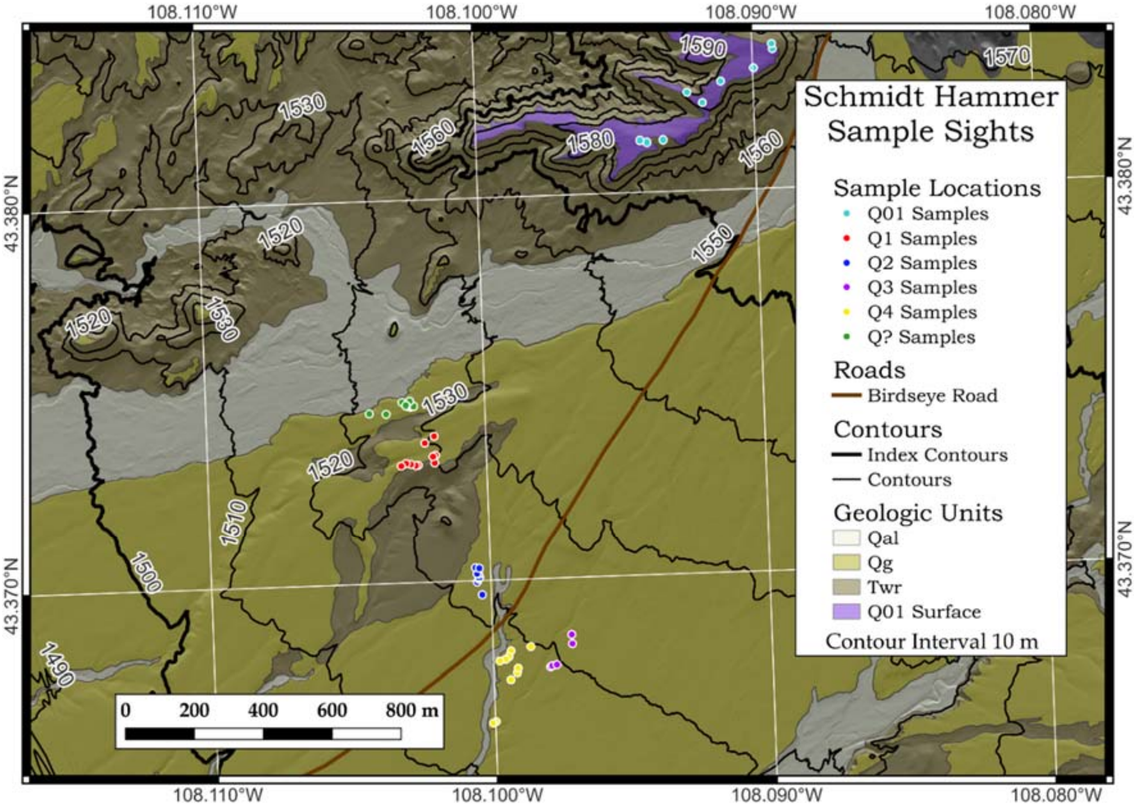

Figure 4-4. Locations for samples that were tested for strength on their weathered surfaces.

Chapter 5: Structural Analysis

This investigation uses new mesoscopic field measurements, as well as previously collected data from geological maps to assess the bedrock structure in the vicinity of the Stagner Creek Fault.

5.1 Methodology

Mesoscopic structural data were assembled from existing geologic maps and new field observations. Prior to field work structural data were digitized from four 1:24,000 scale geologic maps (Thaden, 1978 & 1980). The measurements obtained strike and dip of bedding, fault locations, and fault orientations which were digitized using the program Geologic Map Data Extractor (GMDE; Allmendinger, 2020). Newly acquired mesoscopic measurements would be bedding attitudes, joints, and full kinematics on faults if possible. Figure 5-1 shows the overall map area for the field site with specific locations where new data would be useful.

Data Collection

Mesoscopic field data successfully collected at the field site include attitudes of bedding and jointing, as well as micro fault data (fault strike, dip, slip line rake, and sense of slip). Of the areas of spare data indicated in Figure 5-1, adequate data were acquired in areas 1 and 2. Area 3 was investigated, but no data could be acquired, even when resorting to digging, as this area was mostly loose, friable siltstone that did not display bedding features. Areas 4 and 5 were not thoroughly investigated due to time constraints. Area A was investigated for bedding orientation accuracy and additional data were recorded here. This helps by getting a more precise direction of dip for the overall bedding within the field site. Any anomalies will be examined. A fault located in area A in the existing map data was not found while in the field but could have been missed as inclement weather cut field days short while in this area.

5.2 Structural Data Results

West Cross Section

With the combined map and newly acquired mesoscopic data, a cross section was developed for the western section, labeled cross section O1, of the map area in order to make sense of the pocket of data that deviated from the regional bedding orientation found in area A in Figure 5-1. The cross section can be seen in Figure 5-8. In this cross section, the Wind River formation is projected downward using the dip data measured at the surface. The location indicated in the cross section where the dip of bedding changes direction is a key point in this investigation, and it indicates that a structure has deformed this area locally.

Bedding for West Cross Section (O1)

A stereonet for bedding, Figure 5-3, was developed to display the poles to bedding for all data included in cross section O1, Figure 5-8. The cylindrical fit (Pi-plot) of the bedding poles suggests a sub-horizontal fold hinge with a trend of 282 degrees. Orthogonal to the fold hinge, the local direction of horizontal shortening is NNE-SSW, and this motivated the orientation of the cross section in Figure 5-8.

The abrupt change in the direction of dip near the fault suggests local contraction and therefore the formation of a syncline which is portrayed in the Wind River formation at depth beneath the fault. The main structure within the Owl Creek Mountains north of the field site is a large anticlinorium that was thrusted in the relative south direction and has an axial trace in the relative east/west directions. This pattern of structure is similar with the orientation of the deformation found in the Wind River formation as the hinge of this fold, although extremely broad, also runs in the relative east and west directions.

Joint Planes in Western Field Area

Fracture and joint planes are plotted in Figure 5-4. These are observed in competent lithologies (sandstone and conglomerate beds). Two sub-vertical sets are observed: one generally striking E-W, and one striking N-S. These fracture sets are interpreted as “strike joints” and “dip joints”, respectively, as shown in Figure 5-7. Based on this interpretation, strike-joints result from bending of competent layers and open co-axial with the maximum horizontal stress (approximately N-S) – since this is a contractional tectonic setting, this is likely the maximum principal stress, too. The dip-joints open in the direction of minimal horizontal stress (approximately E-W). These interpreted stress orientations show general coherence with the finite strain orientations indicated by the Pi-plot shown in Figure 5-3.

Fault Kinematics in the Western Field Area

Micro faults were observed in the western area of the field site. All micro faults have a reverse sense of motion and an upper block direction of motion oriented relatively north/south, along with different degrees of oblique slip. In addition to the fault plane orientations and overall sense of shear, slickenline lineations were also measured. These data were kinematically analyzed using a geometric summation (Marrett & Allmendinger, 1990) to infer the orientation of infinitesimal strain axes represented by the ensemble of faults. In the diagram, axis #1 represents the infinitesimal elongation direction oriented sub-vertical, while axis #3 represents the infinitesimal shortening direction oriented N-S. This is shown in Figure 5-5. Fault kinematic data are compatible with the poles to bedding and joint planes data seen in Figures 5-3 and 5-4 respectively.

East Cross Section

A cross section, labeled O2, was developed solely from the existing map data from the 4 USGS geologic maps (Thaden, 1978 and 1980) and is shown in Figure 5-9. No additional structural data was taken in the field. Cross section O2 does have a lower confidence level in its contents, but the basic bedding structure can still be ascertained. The Stagner Creek Fault, with the newly developed DEMs, was able to be traced far enough east to be recorded in this cross section. There are also opposing dip directions in the cross section implying light deformation. However, the bedding is not well constrained as it was in cross section O1 and there do not appear to be any abrupt changes in bedding attitude that may indicate a change in dip direction at the location in the cross section where the fault appears. The conclusion here is that the location of the fault is incorrect or there are not any mesoscopic structural measurements in this vicinity indicating the fault is nearby. Since no new structural data was taken in the eastern area, stress and strain information is absent here.

Bedding for East Cross Section O2

A stereonet for bedding, Figure 5-6, was developed to display the poles to bedding for all data included in cross section O2 and is seen in Figure 5-9. The stereonet agrees with the cross section on opposing directions of dip. The hinge of the fold to this deformation is oriented in the northwest and southeast directions. The deviation in relation to the western data is about 16 degrees rotated in the clockwise direction.

Chapter 5 Figures

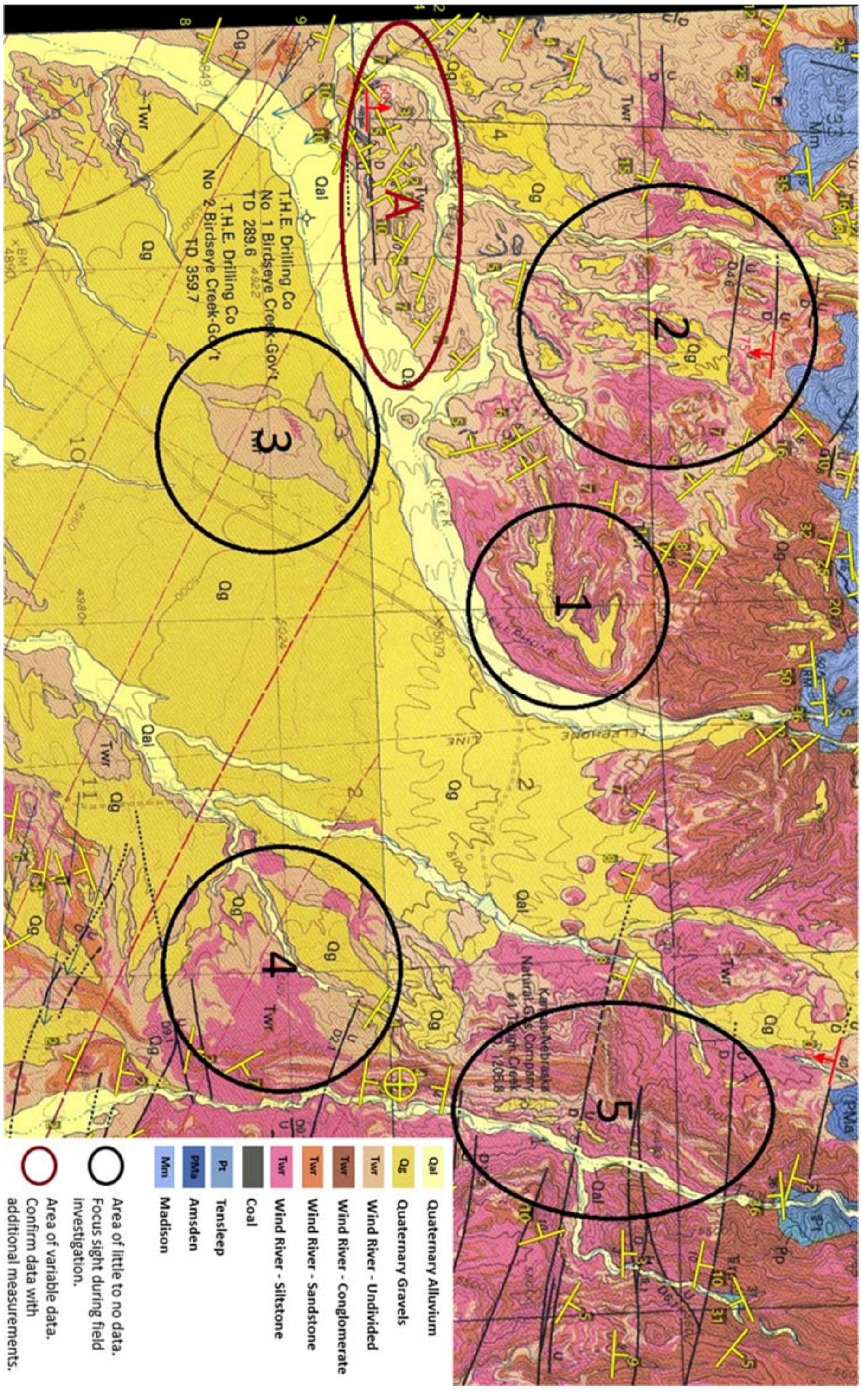

Figure 5-1. The suggested field site focus areas. Taken and adapted from USGS geologic maps GQ-1439 and GQ-1537 (Thaden 1978, 1980).

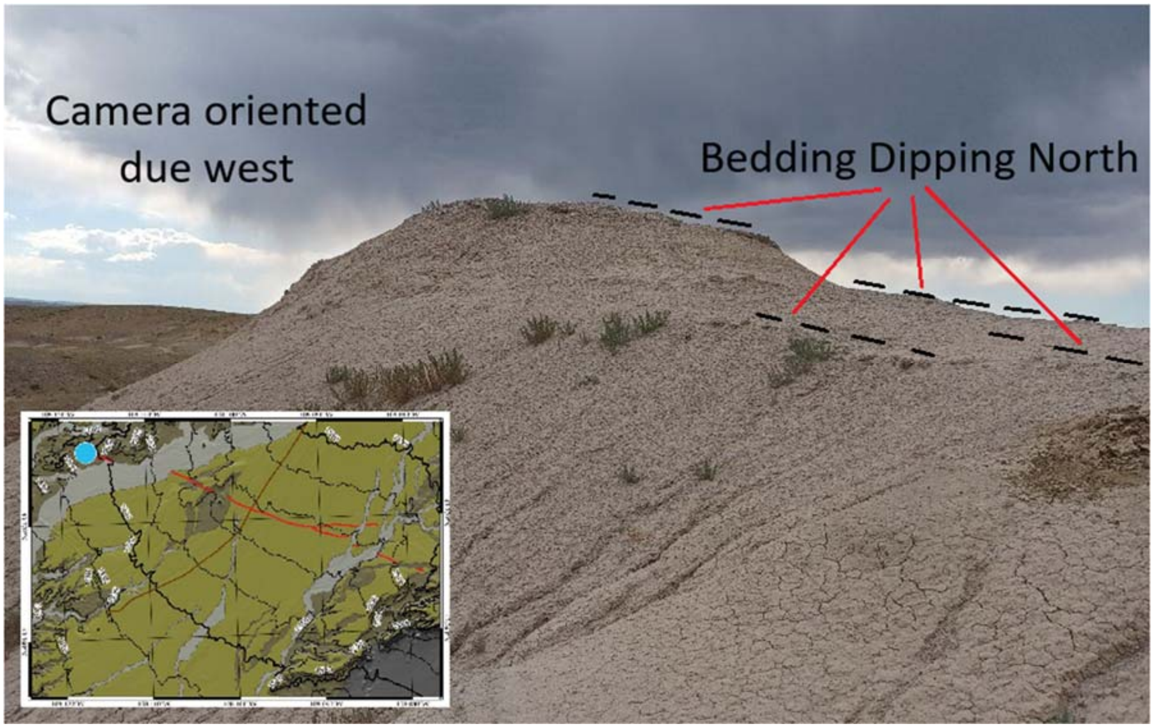

Figure 5-2. This is a photograph of siltstone bedding dipping north within region A of Figure 5-1. The map is from Figure 1-2 with a blue dot indicating the photograph location.

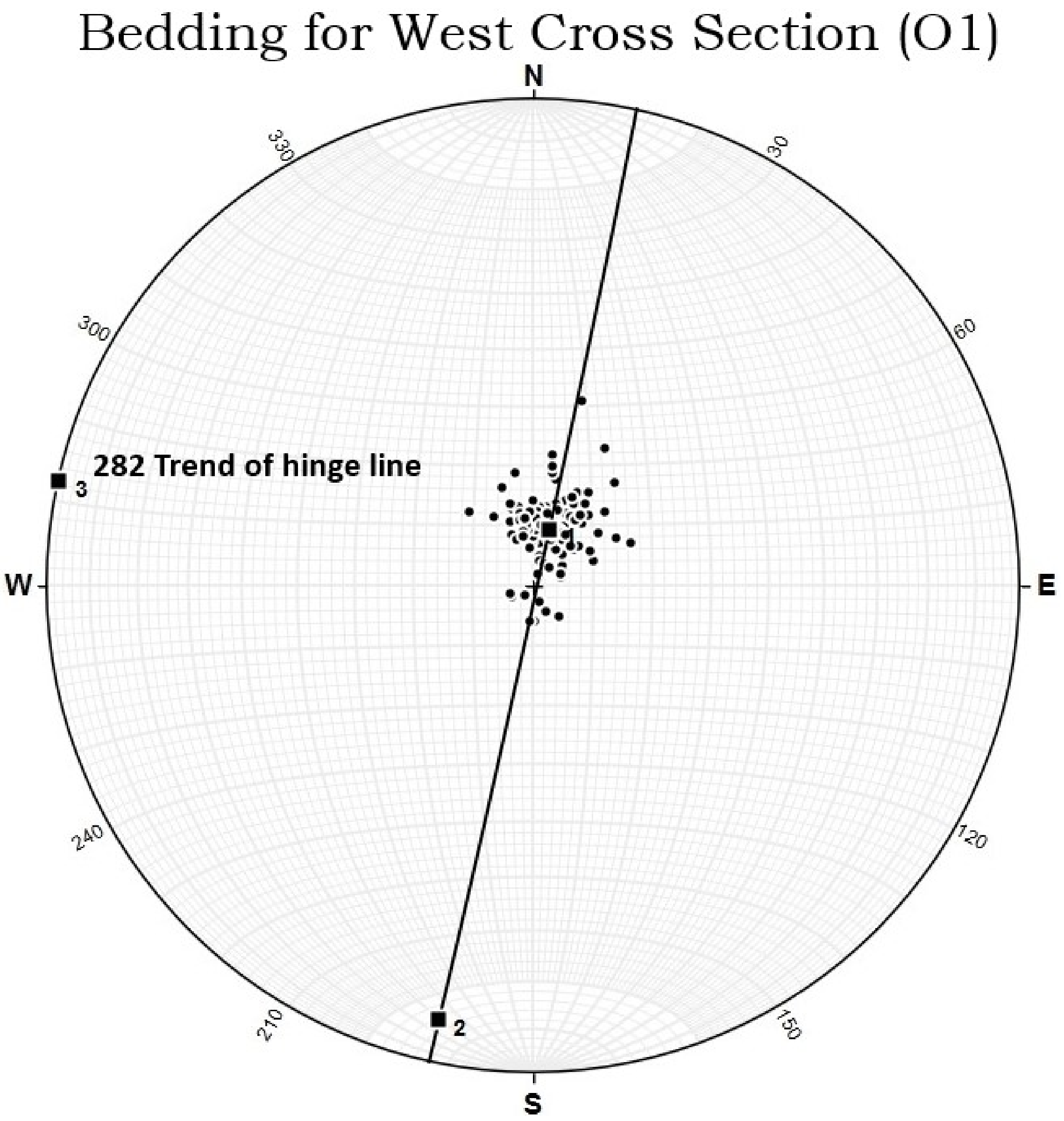

Figure 5-3. This data is a pi diagram of poles to bedding with a line of best cylindrical fit for the data used in cross section O1. Contraction occurred in the NNE-SSW directions.

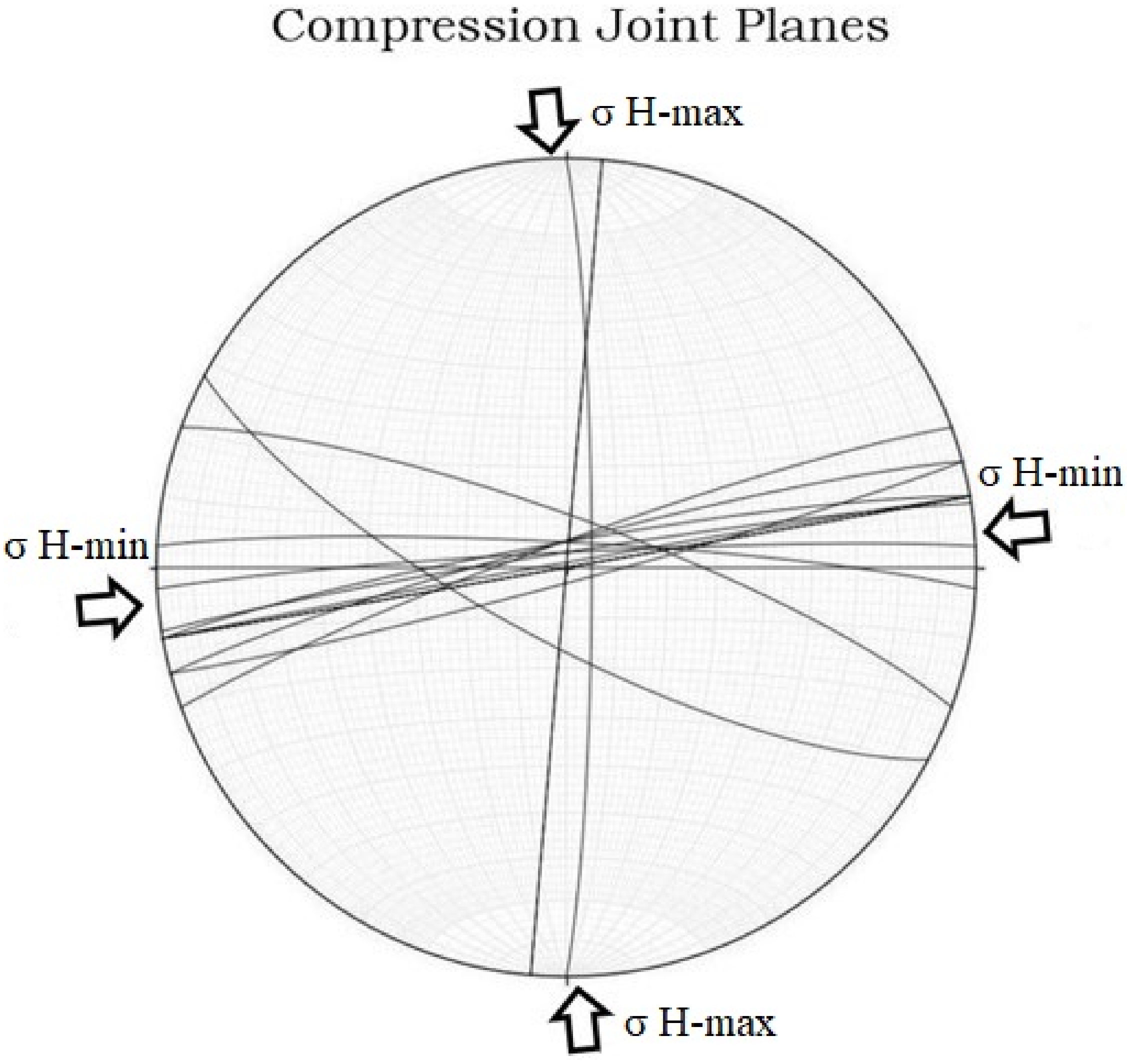

Figure 5-4. This is a pi diagram of joint planes for the west side of the field area containing cross section O1. Notice how the majority of these planes are grouped in a similar orientation.

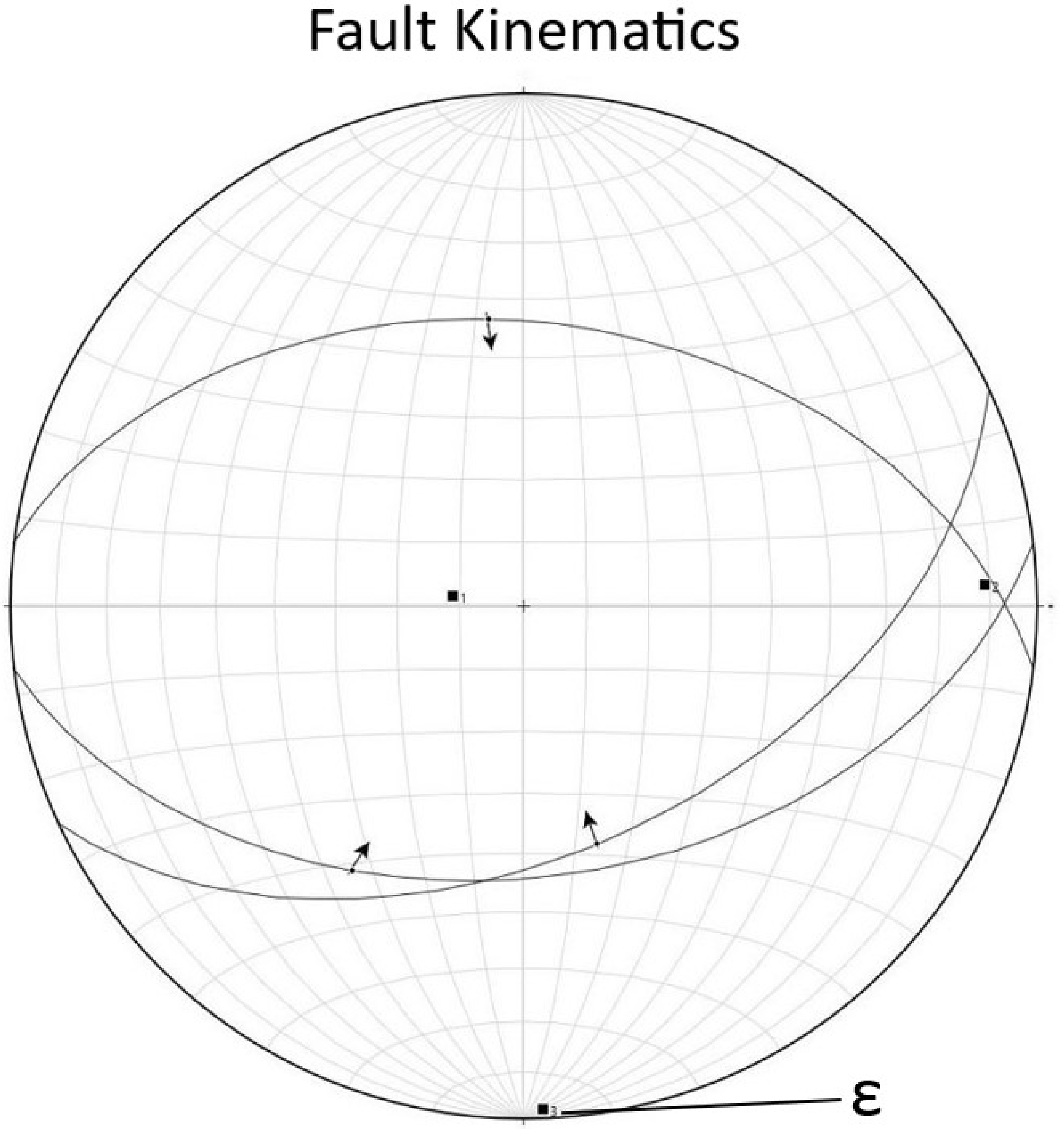

Figure 5-5. This is a pi diagram of fault kinematic data for three reverse micro faults found just west of region 1 in Figure 5-1. Notice how the slip vectors (arrows) on the upper blocks align relatively north/south. Axis 1 (vertical) represents the elongation direction while axis 3 represents ε, the shortening direction.

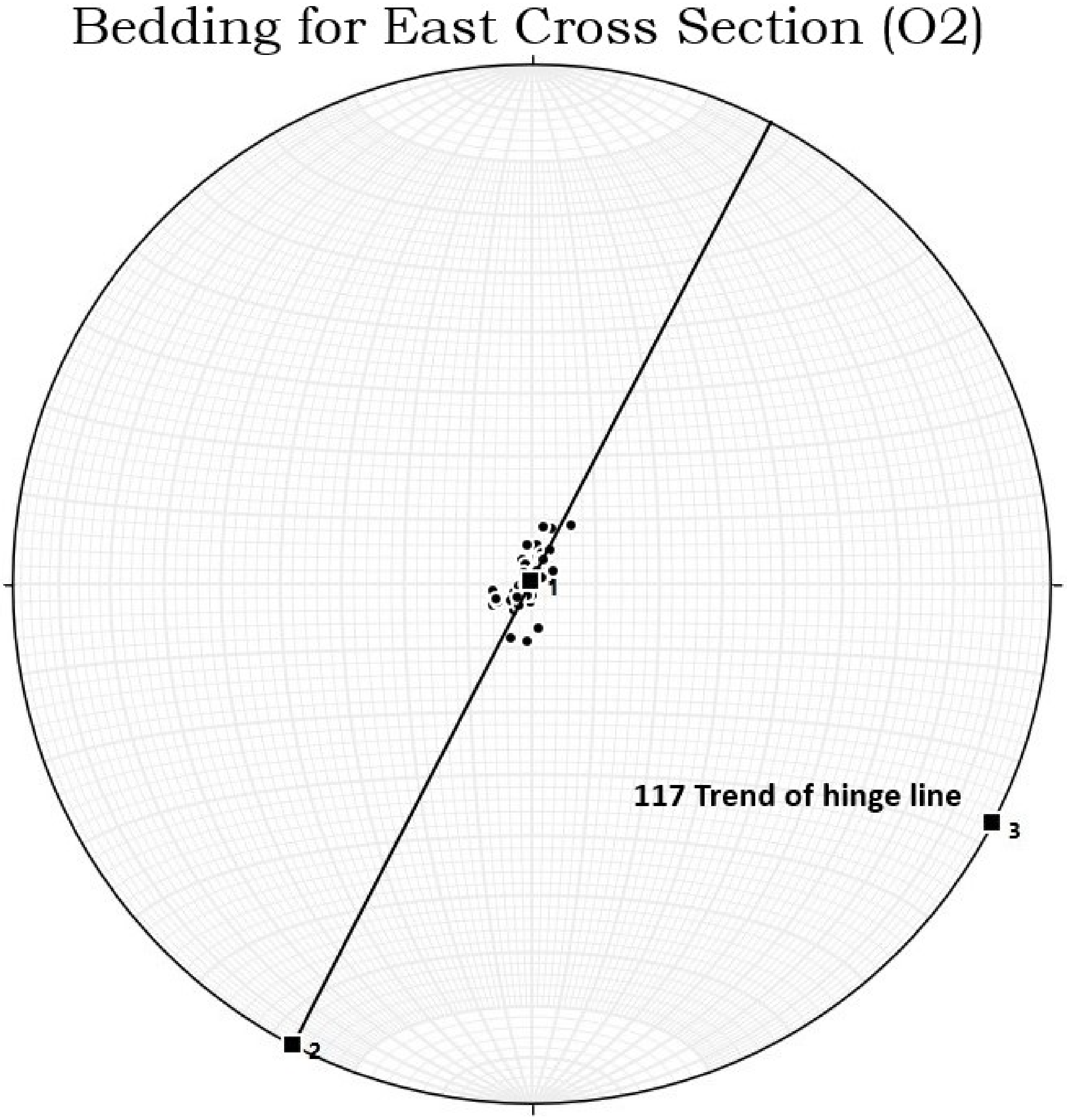

Figure 5-6. This is a pie diagram of polls to bedding with a line of best cylindrical fit for the data used in cross section O2. Contraction occurred in the NNE-SSW directions.

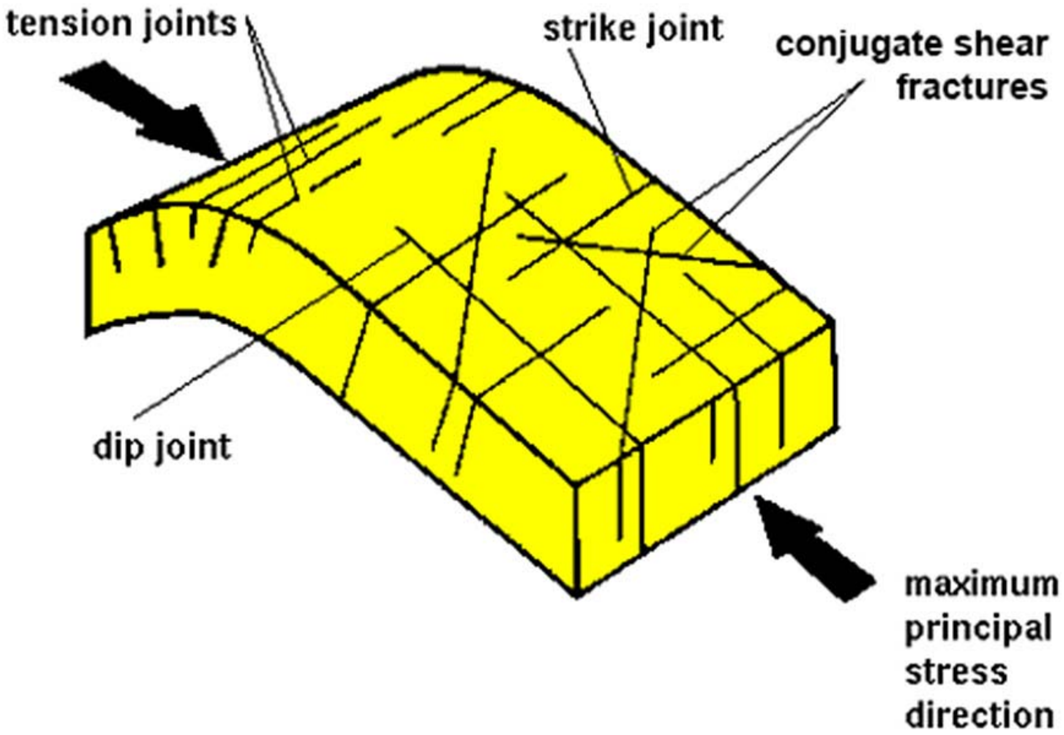

Figure 5-7. Block diagram displaying the various joint sets and the max principal stress direction of a basic fold.

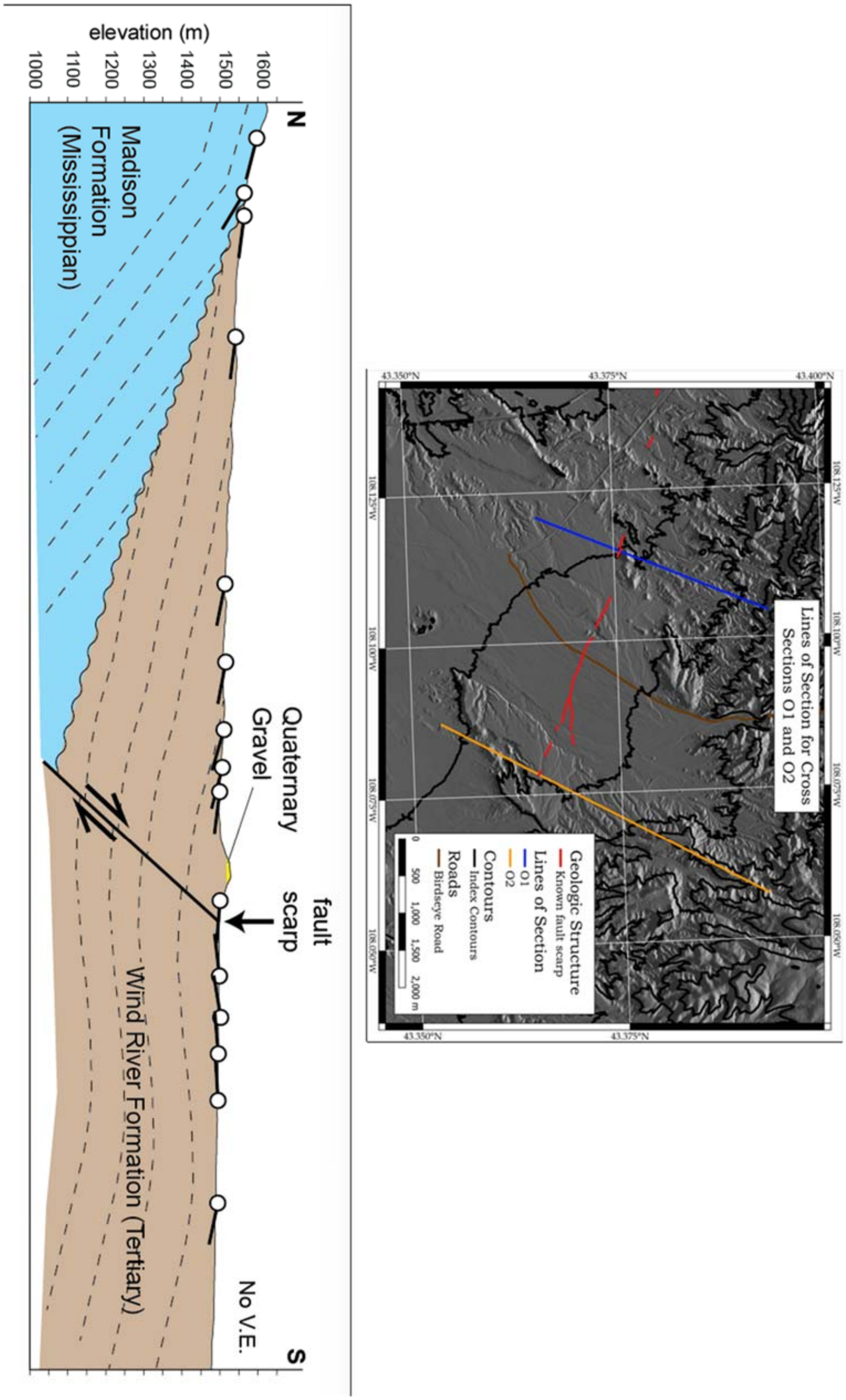

Figure 5-8. Cross Section O1. The map extent is similar to that of Figure 1-2 but the geologic units were removed in order to clearly see the path of the lines of section.

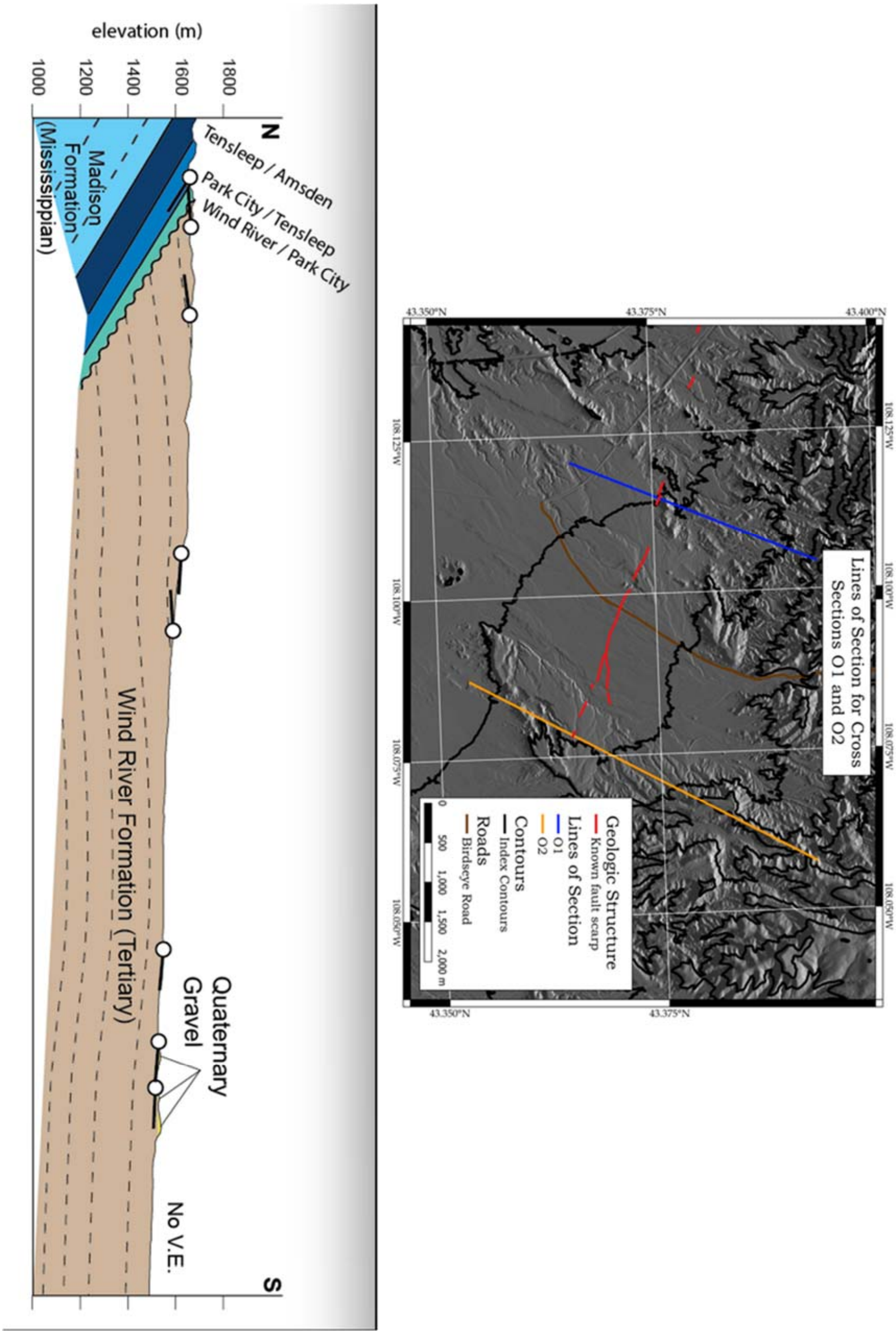

Figure 5-9. Cross Section O2. The map extent is similar to that of Figure 1-2 but the geologic units were removed in order to clearly see the path of the lines of section.

Chapter 6: Discussion and Conclusion

6.1 Integration of Results and Discussion

After examining the various data, there is a compelling argument to be made for the sense of slip of the Stagner Creek Fault. The lineament found in the USGS 1 meter DEM on the west side of Birdseye Creek in Figure 3-3 cannot be ignored as it not only has the same orientation as the Stagner Creek Fault but they are more-or-less colinear. The structural data taken in the field as well as borrowed from Thaden's quadrangle maps both indicate an area of deformation that contains opposing dip directions very near where the fault across the creek has been identified at the surface. The fact that the lineation in Figure 3-3's DEM and the change in direction of dip in the cross section in Figure 5-8 happen to be at precisely the same location can only mean that this is a continuation of the Stagner Creek Fault in the western direction. Unlike the known trace of the fault found in the Geomatrix report, this location is one with bedding planes that are easily visible and measurable. If warping of bedding exists here as presented in Figure 5-8, it can be assumed that warping of bedding exists at the fault's location on the eastern side of Birdseye Creek. Cross section O2 in Figure 5-9 also shows areas of dip direction change toward the east that could coincide with warping of bedding. The quadrangle maps (Thaden 1978, 1980) show multiple faults cutting across the area within this line of section. However, the trace of the Stagner Creek Fault has not been confirmed this far east and therefore, there is no evidence linking this fault to deformation in this area of the map.

The DEMs were also an aid in locating areas to test for strength of weathered rock. Most of the areas that were tested had already been identified in the Geomatrix report, but other higher gravel surfaces were identified for possible testing before surface Q01 (Figure 4-2) was settled on. The Geomatrix report had also identified relative ages linking soils to gravel surface elevations. As mentioned previously, the use of DEMs made it possible to see the fault trace through surface Q5 which proves that the fault is younger than surface Q5 and older than the Quaternary alluvium of Q6 seen in Table 3-1. If surfaces Q2, Q3, and Q4 are grouped together in Figure 4-3, it reinforces the ages of the gravel surfaces relative to each other as the data shows a similar trend in exposure time as it does in the soil development from the Geomatrix report.

Surface Q? remains undistinguished in terms of which surface it is. When relating the scarp heights to the other surfaces, it aligns best with surface Q3 while the Schmidt hammer data points to a surface that is in between the ages of surfaces Q1 and Q2. As mentioned before, it is believed that debris from the higher nearby Q1 surface has shed into surface Q? and skewed the data toward an older age that what should be expected. The only certainty is that it is younger than surface Q1 as it lies adjacent but at a lower elevation. It is also possible that it is its own surface separate from the labeled surfaces in the Geomatrix report and therefore is probably comparable to an age between surfaces Q2 and Q3. This is only an estimated guess from the information gathered in this investigation.

6.2 Conclusion

The first hypothesis stating “the Stagner Creek Fault is a reverse fault” has an abundance of support in favor of it. Cross section O1 in Figure 5-8 shows a break at the surface where opposing dip directions meet. The fault trace at the surface cannot, by itself, be identified as reverse or normal. However, opposing dip directions that dip toward each other suggests down warping of the broader area and therefore contractional processes. Normal faulting is not produced by contractional processes. By eliminating normal faulting, we are left with only one possibility, a reverse sense of motion. Figure 2-11 containing the shallow seismic reflection profile points to the same sense of slip with the upthrown block on the north side of the fault with the fault's dip direction toward the north. North dipping bedding in Figure 5-2 that opposes the regional dip and the pie diagram of poles to bedding in Figure 5-3 displaying contractional processes also point towards a reverse sense of motion on the fault. Therefore, the first hypothesis holds true.

The second hypothesis suggested that the fault cuts across younger aged surfaces than previously found. This was answered in absolute with Figure 3-5's display of the fault scarp within surface Q5. The Geomatrix report found that the fault did not cut across surface Q5. However, this investigation has determined that the report was incorrect.

The third and final hypothesis of this investigation aimed at identifying the trace of the Stagner Creek fault at the surface further than was has been previously mapped by Geomatrix Consultants or in the geologic quadrangle maps in either direction. The DEM in Figure 3-3 displays the fault trace toward the northwest. The trace was assumed to fade out after it encountered the active alluvium produced by Birdseye Creek. This DEM picks the fault trace up as it maintains its trajectory on the other side of the creek. The southeast direction is not as clear as the northwest. First, the DEM in Figure 3-4 needed artificial effects to accentuate the fault scarp, but a faint trace does present itself. Second, the fault trace splays. This could partly explain why the trace here is so faint as the energy causing the break was dispersed. The trace of the fault on the north side of Birdseye Creek is not mapped at all so the third hypothesis remains true for this direction of the fault. In the southeast direction, while new visuals from this investigation have identified the scarp's location, there are multiple fault indicators in the quadrangle maps where this could and probably does connect further to the east.

In reviewing the data found in this investigation in conjuncture with the geologic history of the area, an interesting relationship is observed. In the past, there has clearly been contractional deformation with the onset of the Laramide Orogeny. This created multiple thrust faults that today exist south of the Owl Creek Mountains. One such fault is the Shotgun Butte Thrust. Figure 2-8 displays a cross section of a possible path of the Shotgun Butte Thrust underneath Birdseye Creek. This cross section does not show the thrust breaking the surface. It is a conclusion of the people working on this project that the Stagner Creek Fault is the surface expression of the Shotgun Butte Thrust at Birdseye Creek. Nearby oil wells have been confirmed to show both repeating and inverted units indicating deformation structures at depth. This was not followed up on and furthermore not discussed within the confines of this thesis as it did not directly pertain to confirming the stated hypotheses. However, this could become a separate project.

In discovering that the fault continues toward the northwest, the concerns of the Boysen reservoir and the dam that holds the water back are now slightly elevated. This does not mean that the reservoir is in any immediate danger. This only suggests that if in the slight possibility a seismic event were to occur in this vicinity, damages could be greater and further reaching than expected. Shaking from seismic activity is of some concern, but with the orientation of the fault in the direction of the dam, surface ruptures of the fault pose an altogether different threat. The dam is the obvious object of concern, but hydrocarbon contamination of the water table and therefore the reservoir from nearby oil wells is also possible.

From past events and the relative age dates of the gravel surfaces shown in Table 3-1, earthquake events on this fault occur once every 10 ka. The Q5 Quaternary gravel is the youngest surface the fault cuts across ranging from 1-7 ka. This suggests we are at least 3 ka away from the next event on the Stagner Creek Fault. If a seismic event does occur, a magnitude 6.3 quake estimated by using moment magnitude vs maximum displacement (Wells & Coppersmith, 1994) shown in Figure 3-6 is possible.

Future investigations could focus on the eastern area, primarily around where cross section O2 in Figure 5-9 may encounter discrepancies in dip direction. Pockets of mesoscopic field measurements will need to be acquired to carry this out. There are numerous faults found in quadrangle map GQ-1439 (Thaden, 1978) that could also be investigated. Photogrammetry with UAS flights proved useful in this investigation and could be a further aid in the extended areas. Although expensive, radiometric dating could support the soil dating techniques from the Geomatrix report and the Schmidt hammer work from this investigation.

References

Abousaif, A., (2012). Quaternary Deformation in the Northwestern Wind River Basin, Wyoming (Master's Thesis). University of Missouri

Allmendinger, R.W., (1992). Fold and thrust tectonics of the western United States exclusive of the accreted terranes. B.C. Burchfiel; P.W. Lipman; & M.L. Zoback (Eds.) *The Cordilleran Orogen: Conterminous U.S.* (pp. 583-607). Geological Society of America, Inc.

Allmendinger, R.W., (2020). *Geologic Map Data Extractor (GMDE)*. Retrieved December 5, 2024 from https://www.rickallmendinger.net/gmde

Bader, J.W., (2018). Structural inheritance and the role of basement anisotropies in the Laramide structural and tectonic evolution of the North American Cordilleran foreland, Wyoming. *Lithosphere. Vol. 11(1),* pp. 129-148. https://doi.org/10.1130/L1022.1

Blackstone, D.L., Jr., (1990). Rocky Mountain Foreland Structure Exemplified by the Owl Creek Mountains, Bridger Ranger, and Casper Arch, Central Wyoming. *WGA 41st Annual Field Conference Guidebook: Wyoming Sedimentation and Tectonics.* pp. 151-166.

Blakely, R.C., (2013). Using paleogeographic maps to portray Phanerozoic geologic and paleotectonic history of western North America. *Search and Discovery, 30267*

CIG Exploration, (1978). Birdseye Creek 1, 773 FNL and 1813 FEL (NW NE) Section 4 Township 39 North Range 94 West, CIG Exploration

Delisle, C., (2016). Geomorphological and Geophysical Evaluation of Quaternary Intraplate Deformation in the Northern Wind River Basin, Wyoming. [Unpublished Bachelor's Thesis]. University of Missouri.

Fonstad, M.A., et al, (2012). Topographic Structure from Motion: A New Development in Photogrammetric Measurement. *Earth Surface Processes and Landforms. Vol. 38,* pp. 421-430. https://doi.org/10.1002/esp.3366

Geomatrix Consultants, Inc., (1988). Seismotectonic Evaluation of the Northwestern Wind River Basin. Project No. 1350A. Geomatrix Consultants, Inc.,

Glass, G.B., (1986). A geologic tour of Wyoming from Laramie to Lander, Jackson and Rock Springs. Wyoming Geologic Survey. (Public Information Circular No. 27)

Gomez, F., Abousaif, A., & Sandvol, E., (2016). *Re-evaluation of late Quaternary deformation in the northern Wind River Basin, Wyoming*. Paper presented at the 7th International INQUA Meeting on Paleoseismology, Active Tectonics and Archeoseismology, May 30 to June 3, 2016, Crestone, Colorado, USA.

Goudie, A.S., (2016). Quantification of rock control in geomorphology. *Earth-Science Reviews. Vol. 159*, pp. 374-387. https://doi.org/10.1016/j.earscirev.2016.06.012

Hanks, T.C., et al, (1984). Modification of Wave-Cut and Faulting-Controlled Landforms. *Journal of Geophysical Research. Vol. 89(B7),* pp. 5771-5790. https://doi.org/10.1029/JB089iB07p05771

Hanks, T.C., (2000). The age of scarplike landforms from diffusion-equation analysis. J.S. Noller; J.M. Sowers; & W.R. Lettis (Eds), *Quaternary geochronology:*

Methods and applications (Vol. 4, pp. 313-338). American Geophysical Union. https://doi.org/10.1029/RF004p0313

Horton, B.K., et al, (2022). Broken foreland basins and the influence of subduction dynamics, tectonic inheritance, and mechanical triggers. *Earth-Science Reviews. Vol. 234*, https://doi.org/10.1016/j.earscirev.2022.104193

Jia, H. et al., (2021). Fan-delta facies architecture, morphological evolution and sediment delivery in the Oligocene Dongying formation of the Nanpu Sag, Bohai Bay Basin, China. *Australian Journal of Earth Sciences. Vol 68(8),* pp. 1201-1214. https://doi.org/10.1080/08120099.2021.1917453

Keefer, W.R., (1965). *Geological Survey Professional Paper No. 495-A: Stratigraphy and Geologic History of the Uppermost Cretaceous, Paleocene, and Lower Eocene Rocks in the Wind River Basin, Wyoming.* U.S. Government Printing Office: Washington DC. Retrieved from: https://pubs.usgs.gov/pp/0495a/report.pdf

Keefer, W.R., (1970). *Geological Survey Professional Paper No. 495-D: Structural Geology of the Wind River Basin, Wyoming.* U.S. Government Printing Office: Washington DC. Retrieved from: https://pubs.usgs.gov/pp/0495d/report.pdf

Marrett, R. A., & Allmendinger, R. W., (1990). Kinematic analysis of fault-slip data. *Journal of Structural Geology, Vol. 12*(8), pp. 973-986. https://doi.org/10.1016/0191-8141(90)90093-E

Matthews, J.A., & Winkler, S., (2022). Schmidt-hammer exposure-age dating: a review of principles and practice. *Earth-Science Reviews. Vol. 230*, https://doi.org/10.1016/j.earscirev.2022.104038

Neal, C.R., (n.d.). Non-plunging fold. https://www3.nd.edu/~cneal/PlanetEarth/Lab-Structural/Folds.html

Niedzielski, T. et al., (2009). A minimum sample size required from Schmidt hammer measurements. *Earth Surface Processes and Landforms. Vol. 34* pp. 1713-1725. https://doi.org/10.1002/esp.1851

Plateforme LIDAR, (2024). 3DMASC. https://lidar.univ-rennes.fr/en/3dmasc#p-65

Polun, S.G., (2021). *pyScarpFit.* https://github.com/seanpolun/pyScarpFit/

Potter, M.R., (2022). Active deformation of the south Granite Mountain Fault system: Reactivated compressional faults vs. extensional overprinting (Master's Thesis). University of Missouri.

Poole, R.W., & Farmer, I.W., (1980). Consistency and repeatability of Schmidt hammer rebound data during field testing. *Int. J. Rock Mech. Min. Sci. Geomech. Abstr. Vol. 17*, pp. 167–171. https://doi.org/10.1016/0148-9062(80)91363-7

Rock Joints Terminology, (2014). https://www.geologyin.com/2014/10/joints-terminology-brittle-deformation.html

Soister, P.E., (1968). *Geological Survey Professional Paper No. 594-A: Stratigraphy of the Wind River Formation in South-Central Wind River Basin, Wyoming.* U.S.

Government Printing Office: Washington DC. Retrieved from: https://pubs.usgs.gov/pp/0594a/report.pdf

Thaden, R.E., (1978). *Geologic Map of the Bonneville quadrangle, Fremont County, Wyoming* (Geologic Quadrangle Map GQ-1439). Scale 1:24,000. U.S. Geological Survey. Retrieved from https://ngmdb.usgs.gov/mapview

Thaden, R.E., (1980). *Geologic Map of the Guffy Peak quadrangle, showing chromolithofacies in the Wind River formation, Fremont and Hot Springs Counties, Wyoming* (Geologic Quadrangle Map GQ-1527). Scale 1:24,000. U.S. Geological Survey. Retrieved from https://ngmdb.usgs.gov/mapview

Thaden R.E., (1980). *Geologic Map of the Birdseye Pass quadrangle, showing chromolithofacies and coal beds in the Wind River formation, Fremont and Hot Springs Counties, Wyoming* (Geologic Quadrangle Map GQ-1537). Scale 1:24,000. U.S. Geological Survey. Retrieved from https://ngmdb.usgs.gov/mapview

Thaden, R.E., (1980). *Geologic Map of the Picard Ranch quadrangle, showing chromolithofacies and coal beds in the Wind River formation, Fremont County, Wyoming* (Geologic Quadrangle Map GQ-1539). Scale 1:24,000. U.S. Geological Survey. Retrieved from https://ngmdb.usgs.gov/mapview

Viles, H. et al., (2011). The use of the Schmidt hammer and equotip for rock hardness assessment in geomorphology and heritage science: a comparative analysis. *Earth Surface Processes and Landforms. Vol. 36* pp. 320-333. https://doi.org/10.1002/esp.2040

Wallace, R.E., (1977). Profiles and Ages of Young Fault Scarps, North-Central Nevada. *GSA Bulletin Vol. 88(9),* pp. 1267-1281. https://doi.org/10.1130/0016-7606(1977)88<1267:PAAOYF>2.0.CO;2

Wells, D.L., & Coppersmith, K.J., (1994). New Empirical Relationships among Magnitude, Rupture Length, Rupture Width, Rupture Area, and Surface Displacement. *Bulletin of the Seismological Society of America. Vol. 84(4)* pp. 974-1002. https://doi.org/10.1785/BSSA0840040974

Wise, D.C., (1963). Keystone faulting and gravity sliding driven by basement uplift of Owl Creek Mountains, Wyoming. *Bulletin of the American Association of Petroleum Geologists. Vol. 47(4),* pp. 586-598. https://doi.org/10.1306/BC743A67-16BE-11D7-8645000102C1865D

Wyoming Geological Association, Technical Studies Committee, (1964). *Highway Geology of Wyoming: Road Logs of the Highways, Including Points of Geologic, Economic, Historic, and Scenic Interest.* Wyoming Geological Association